

---

# **An Integrated CFD/Experimental Analysis of Aerodynamic Forces and Moments**

---

John E. Melton, David D. Robertson, and Seth A. Moyer  
Ames Research Center, Moffett Field, California

August 1989



National Aeronautics and  
Space Administration

**Ames Research Center**  
Moffett Field, California 94035

## SUMMARY

Aerodynamic analysis using computational fluid dynamics (CFD) is most fruitful when it is combined with a thorough program of wind tunnel testing. The understanding of aerodynamic phenomena is enhanced by the synergistic use of both analysis methods. This report describes a technique for an integrated approach to determining the forces and moments acting on a wind tunnel model by using a combination of experimentally measured pressures and CFD predictions. The CFD code used was FLO57 (an Euler solver) and the wind tunnel model was a heavily instrumented delta wing with  $62.5^\circ$  of leading-edge sweep. A thorough comparison of the CFD results and the experimental data is presented for surface pressure distributions and longitudinal forces and moments. The experimental pressures were also integrated over the surface of the model and the resulting forces and moments are compared to the CFD and wind tunnel results. The accurate determination of various drag increments via the combined use of the CFD and experimental pressures is presented in detail.

## NOMENCLATURE

<u>Symbol</u>	<u>Description</u>
$c$	local chord
$C_D$	drag coefficient
$C_{D0}$	value of drag at zero lift
$C_{FLam}$	laminar skin friction coefficient
$C_{FTurb}$	turbulent skin friction coefficient
$C_L$	lift coefficient
$C_M$	pitching moment coefficient
$C_{M0}$	value of pitching moment at zero lift
$C_p$	coefficient of pressure
$M$	free-stream Mach number
$Re$	Reynolds number
$x$	chordwise distance from leading edge
$\alpha$	angle of attack

## INTRODUCTION

Wind tunnel testing requirements for instrumentation, propulsion simulation hardware, and support systems are often in conflict with one another for physical space inside a complicated wind tunnel model. As a result, incremental forces and moments are often derived from integrated experimental pressure data because of the difficulty of directly measuring the forces and the moments in question. This approach is typically taken in the study of propulsion-related phenomena such as inlet spillage and nozzle boat-tail drag. This method is usually suspect because of the relatively small number of pressure measurements normally available over complex three-dimensional surfaces. In addition, a separate test must be conducted to provide the baseline force and moment characteristics to which the incremental forces are added. The error inherent in the individual elements of this approach contributes to skepticism regarding the final data and makes validation difficult.

The first part of this report presents a detailed comparison between computational fluid dynamics (CFD) predictions and wind tunnel data for surface pressure distributions and longitudinal forces and moments. The effects of numerical discretization were explored by using three computational grids of varying density. The large number of wind tunnel pressure taps also allowed side-by-side colored surface pressure contour comparisons to be made between the experimental and computational results. This technique was useful for highlighting slight discrepancies in wing pressure distributions that were not noticeable when the traditional  $C_p$  versus  $x/c$  plots were examined.

The second part of this report investigates the feasibility of integrating experimentally measured pressures on a simple configuration to determine the absolute values of forces and moments acting on a wind tunnel model. An integrated approach for accurately determining forces and moments using both wind tunnel results and CFD predictions is described. The success of this combined approach to force and moment calculations provides a limited validation of the pressure integration methodology and demonstrates that the technique may be useful for assessing the forces and moments on individual components.

## MODEL GEOMETRY

The wind tunnel model was a full-span, delta-wing model with  $62.5^\circ$  of leading-edge sweep. A plan view showing pressure tap locations is given in figure 1. The simple geometry and large number of pressure taps (287) made it an ideal candidate for both the CFD code validation and the pressure integration analysis. To accommodate other test requirements, the model was designed to be supported near the wingtips. As a result, there was a fairly large gap between the 10th and 11th chordwise rows of pressure taps. In addition, a few geometric modifications were made to the wind tunnel model before the present test to assist in the pressure integration study and to assure tunnel compatibility. Inlets on the lower surface were faired over, and a sting shroud was added that covered a small portion of the upper surface and some of the associated pressure taps. Outside these regions, the model had an excellent pressure tap distribution on both the upper and lower surfaces.

The geometry used for the CFD analysis and post-test pressure integrations was obtained in a panel code type input format. It consisted of three networks containing the forward wing region, the aft wing region, and the sting shroud. There were 12 span stations with 27 chord points to define each airfoil. This definition was assumed to accurately duplicate the contours of the wind tunnel model. This assumption did not hold near the faired inlet locations.

## **WIND TUNNEL TEST**

The model was tested in the Ames Research Center's 11- by 11-Foot Transonic Wind Tunnel. The test covered a wide range of Mach numbers and model attitudes. This report will use only the longitudinal data obtained at  $M=0.8$ ,  $Re/ft = 2.5$  million;  $M=0.7$ ,  $Re/ft = 2.5$  million; and  $M=0.4$ ,  $Re/ft = 2.0$  million.

## **CFD ANALYSIS**

### **Grid Generation**

An OH-grid topology was chosen for this study. It can easily handle wings with low taper ratios or pointed tips, and it provides for an efficient clustering of points along the leading edge. The grid-generation process can be broken down into three steps. In the first step, a commercial CAD/CAM system was used to generate cross sections of the model at specified longitudinal locations (Enomoto, 1983). These cross sections were then redistributed to provide grid clustering in regions of high curvature. Finally, the surface grid at each cross section was extended into the 3-D space surrounding the body. To produce a smooth grid, a two-dimensional, elliptic grid-generation routine was used to create each grid plane. Figure 2 shows a cross-sectional view of one of the grid planes in the fine grid. Since the grids are created at successive longitudinal stations, the sting can be incorporated in a straightforward manner.

Three grids of varying density were used to investigate the sensitivity of the computations to different discretizations. The three model upper surface grids are shown in figure 3. The grid crossover that occurs near the trailing edge in these planform views is not a true crossover, but is a wrapping of grid lines around the double-valued sting surface. Information about the three grids is given in table 1.

### **Flow Solver**

The FLO57 CFD code integrates the Euler equations using A. Jameson's four-stage explicit Runge-Kutta algorithm (James and Baker, 1983). The original program used in this study had been modified by numerous authors and additional modifications were necessary to incorporate the OH-grid topology. Goodsell and Newsome (Goodsell, Madson, and Melton, 1989; Newsome and Kandil, 1987) provide details of the Euler solution strategy and the arguments for the applicability of Euler codes to delta configurations.

## CFD Comparisons

The extensive pressure instrumentation allowed very detailed surface pressure comparisons to be made over the entire span of the model. The lift, drag, and moment coefficients were also compared to the experimental data. Three grids of varying density were run to provide a rough estimate of grid density on solution characteristics. All solutions were run to a minimum of three orders of magnitude convergence in the density residual. Lift, drag, moment, and the number of supersonic points versus iteration were also monitored to ensure converged results. Table 1 provides information about the computational resources required for the FLO57 analysis. The computational run schedule is given in table 2.

The predicted and experimental surface pressure comparisons are shown in figures 4-6, and the resulting force and moment data are presented in figures 7-9. Included with the experimental data and FLO57 predictions are the results of an analysis using PANAIR, a panel method code (Carmichael and Erickson, 1981).

The agreement between the FLO57 and wind tunnel pressure distributions is generally excellent, except in regions where significant viscous effects were to be expected. The pressure distributions shown in figures 4-6 show the ability of the Euler code to predict the details of the inboard pressure distributions, including the magnitude and extent of the leading-edge expansion spikes. At the trailing edge, FLO57 overestimates the amount of pressure recovery. The wind tunnel pressure distributions do not recover to the same level as FLO57 because of boundary-layer displacement effects and trailing-edge separation. The detailed mechanics of the leading-edge vortex formation and the secondary separations of the boundary layer due to the resulting adverse spanwise pressure gradients are also incorrectly modeled by the inviscid Euler code. The effect of these modeling differences on the pressure distributions become significant as the vortex increases in strength along the leading edge. These vortex-boundary layer interactions result in an increasingly poorer  $C_p$  comparison toward the tip. The result of neglecting the physics involved in these important flow-field interactions is clearly seen in the outboard pressure distributions of figures 4h, 5h, and 6f. Increasing the angle of attack strengthens the vortex and increases its interaction with the boundary layer.

The effect of the geometry modifications made to the lower surface inlet fairing can be seen in the lower surface  $C_p$  distributions at the three most inboard stations between  $x/c = 0.2$  to  $0.3$ . This discrepancy remains throughout the entire Mach and a range. The input geometry data set did not accurately reflect the contours of the faired inlet regions.

Although the overall pressure agreements between the computations and wind tunnel were very good, the slope and sign of the moment curves predicted by FLO57 did not correlate well for any of the three Mach numbers investigated, as seen in figures 7-9. The fundamental origin of this difference between the wind tunnel moment curve and the FLO57 and PANAIR predictions was difficult to identify. The fact that this difference persisted even at low lift conditions was especially troubling, because the effects of incorrect vortex modeling, viscosity, and shock waves were not expected to be large for small angles of attack. Studying individual chordwise pressure distributions did not yield any obvious explanations. In order to study the decambering effect of the boundary layer, a turbulent displacement thickness was calculated and was added to the upper and lower surfaces of the medium grid, but did not change the FLO57 moment slope appreciably. A thorough check of the wind tunnel data-reduction system was also made.

The origin of the difference between the FLO57 and wind tunnel moment curves was eventually discovered by comparing the overall computed and experimental pressure distributions. This was accomplished by preparing colored planform views of the model that combined experimental and computational predictions. Half of each wing surface was colored with the experimental pressures, and the other half by the predicted computational pressures (Hermstad, 1989). Each wind tunnel pressure tap was assigned a surrounding area on the wing, and these areas were colored by the  $C_p$  measured at the tap. Each surface cell in the FLO57 grid was similarly colored by the pressure predicted at its center, making a direct comparison between the experiment and computations possible. Although these colored planform comparisons are more qualitative than the traditional chordwise plots, they tend to accentuate overall trend differences. This can be seen by studying figures 10 and 11, which correspond to  $\alpha$ -sweeps at Mach = 0.40 and Mach = 0.80.

Upon close review, it can be seen that the upper surface pressure distributions predicted by FLO57 tend to have a slightly lower pressure extending further aft on the wing. This additional aft loading, when integrated over the entire span, produces a more negative pitching moment and exists even at low lift conditions. Further review of the plots of individual chordwise pressure distributions shows this difference to be small, but to extend over the entire span. It would appear that geometrical inaccuracies in the wing geometry network files, and not viscous effects, are the major source of the computational moment discrepancy.

The effect of the grid density on surface  $C_p$  distributions appeared to be small, but it did increase somewhat near the wingtips. The lift, drag, and moment were also not strongly affected by grid size. Since the agreement between the three grids at Mach = 0.8 was so good, it was decided not to run the expensive large grid at Mach = 0.4 and 0.7.

### Experimental Pressure Integration

The experimental pressure integration scheme used the simple midpoint rule, where an area and unit normal vector were associated with each tap location. A skin friction estimate (discussed in more detail in the following paragraphs) was added to the drag computations to compare the resulting integrated data to the balance data.

Tap areas were determined by placing a panel around each pressure tap. Sides of these panels were positioned at the midpoint between adjacent taps. The unit normal vectors assigned to each area were the unit normals to the surface calculated at the centroid of each panel. These centroids were generally very close to the tap locations.

Since the sting shroud was not pressure-instrumented, it was not modeled in the pressure-integration scheme. Instead, the panel areas of the most adjacent spanwise taps were extended to the model centerline, as illustrated in figure 12.

The integration scheme might have been improved by determining an average unit normal vector over the surface of a panel instead of using that found at the centroid. In addition, a higher order numerical integration method could have been used (Rice, 1983). The midpoint rule was used for this study

because it was the most straightforward and therefore it simplified locating and correcting errors in the integration scheme.

### Skin Friction Estimation

Skin friction increments were applied only to the drag because the skin friction effect on pitching moment was assumed to be negligible. The skin friction coefficients used were the classical incompressible ones listed below (Schlichting, 1979):

$$C_{FTurb} = 0.074/Re^{0.2}$$

$$C_{FLam} = 1.328/\sqrt{Re}$$

Boundary-layer transition from laminar to turbulent was forced near the leading edges of the wings by a transition strip set 1.0 in. streamwise from the leading edge. The drag increment due to this strip was determined to be insignificant. In addition, drag sensitivity to this turbulent transition location (in case the transition strip failed to trip the boundary) was analyzed and was also found to be negligible. Therefore, the above coefficients were determined based on the transition strip location and mean chord.

### Integrated Force and Moment Comparisons

Figures 13-15 show  $C_L$ ,  $C_D$ , and  $C_M$  comparisons of balance, integrated pressures, and integrated pressures plus skin friction. Comparing the three figures shows that the lift curve derived from the integrated pressures agrees very well with the balance data for all three Mach numbers. This is to be expected, since the distribution of integration panels projected onto a plane perpendicular to the lift axis is very good. The only gaps occur at the sting shroud and just inboard of the two wingtip rows.

The pitching moment data also agree quite well. There is a general trend, however, for the integrated pressures to consistently give a more positive pitching moment than that measured experimentally. At higher angles of attack this trend becomes significant.

A possible reason for this discrepancy is the removal of the sting shroud from the integration scheme. The shroud extended 2.9 in. past the trailing edge. At zero angle of attack the surface of the shroud is essentially parallel to the free stream and does not contribute to the frontal area of the model. At higher angles of attack the tail end of the shroud becomes visible to the oncoming flow and subsequently exerts a nose-down moment. The experimental pressure integration failed to capture this nose-down moment.

The balance drag polar and the integrated pressure drag polar do not agree as well as the lift and moment curves. All three Mach numbers analyzed indicate the same trend. The integrated pressures overestimate the drag by a constant increment over the range of lift coefficients. Figures 13-15 show that the shape of the polars agree quite well, but they also show a shift of the integrated pressure polar in the positive direction. Analysis into this drag shift centered on a number of possible causes: (1) inaccurate wind tunnel data, (2) errors in the integration scheme, (3) inaccurate skin friction estimate, (4) errors in geometry used in integration, and (5) inadequate number of pressures on the model surface. These causes were analyzed, and the results are presented in order in the following sections.

1. Inaccurate wind tunnel data: The wind tunnel data was thoroughly examined and all data and corrections appear to be accurate within the limits of the instrumentation ( $\Delta C_D \leq \pm 0.0003$ ).

2. Errors in the integration scheme: Possible errors in the integration scheme were evaluated by examining the unit normal vectors and panel areas assigned to each pressure tap. These values were compared with normal vectors and panel areas previously determined by the test engineer. The earlier values were not used for this study because the manner in which the areas around the sting shroud were computed was unclear. All the values compared very well with only a few minor differences. These differences were not significant enough to account for the drag shift found in the integration.

3. Inaccurate skin friction estimate: The analysis of errors in the skin friction estimate was limited to the turbulent region because only a small portion of flow over the model's surface was laminar. The turbulent estimate is an incompressible solution from Prandtl's 1/7th-power velocity profile (Schlichting, 1979). This relation is the classical turbulent skin friction estimate generally used in conceptual design. A method that incorporates compressibility was proposed by Sivells and Payne (1959). Of course, the largest difference between the two methods is found at Mach = 0.80 where  $C_{F_{turb}} = 0.00316$  for the classical Prandtl method and 0.00293 for Sivells and Payne. Here the skin friction coefficient is reduced by 7.5%. However, a reduction in skin friction of about 50% would be necessary to match the balance.

Also, as opposed to using a Reynolds number based on mean chord, the planform was divided into eight chordwise strips of the same width. The skin friction for each strip based on its chord was determined. The total was then arrived at by summing the skin friction for each strip. The error associated with this was about 1%. Therefore, the error in skin friction caused by its estimation technique was not considered large enough to account for the drag difference seen in figures 13-15.

4. Errors in geometry used in integration: The most obvious geometrical difference between what the balance measured and the manner in which the integration was performed was the sting shroud. As mentioned earlier, there were no pressures available for integration over the surface of the shroud. Instead, the sting shroud was removed from the integration geometry, and each pressure tap directly outboard of the shroud was assigned an area that extended to the model centerline.

If the total drag measured by the balance is thought of as the sum of the surface skin friction and the drag component of pressure forces, then a systematic approach may be taken for determining the effect of removing the sting shroud from the integration. First, the increase in skin friction between the total wetted area with and without the sting shroud is calculated. The difference in total drag is  $\Delta C_D = 0.0002$ . This is approximately the resolution of the balance. Second, the effect of removing the shroud from the integration of pressure forces is estimated. The model geometry indicates that the surface of the

sting shroud has no aft-facing area. In addition, the final balance forces included base and cavity corrections. In other words, any axial force due to base and cavity areas was removed from the final forces and moments recorded in the wind tunnel. Therefore, the pressure forces on the sting shroud produced no axial force in the final balance data.

In comparison, the geometry used for the experimental pressure integration does have aft-facing surface area in the region that was occupied by the shroud. This additional aft-facing area in the integration geometry contributes to the axial force. Therefore, if the axial force caused by this area is removed from the integration, a reasonable estimate for the shroud's effect can be determined.

Another method for determining the effect of removing the shroud on the integration of pressure forces is to use the computational solution. The FLO57 solution contained the sting shroud. If the surface grid is modified so that the cells directly outboard of the shroud are extended to the model centerline in the same way as the experimental panels were, then a good estimate for the drag differences with and without the shroud may be obtained.

Results from both methods are presented in figure 16 for Mach = 0.80. Values found using the experimental pressures are then shown combined with the data in figure 17. The figure demonstrates that the shroud correction does improve the correlation between the balance and integration curves, but it also indicates that a sizable shift in drag still remains unaccounted for. No other major geometric differences are present to account for this drag shift.

5. Inadequate number of integration pressures: To integrate the drag accurately requires a good distribution of small integration panels that have significant components of their surface normals acting in the forward and aft direction. Frontal areas are small in comparison to planform areas, and large pressure gradients exist that cannot be adequately captured by a few taps. This wind tunnel model was chosen for this study because of its relatively large number of pressure taps and simple shape. Despite this, the drag still could not be estimated accurately. Economic and instrumentation limitations constrain the actual number of pressure taps that may be incorporated into a model. Increasing the number of taps ad infinitum on a wind tunnel model to integrate pressures for the drag therefore simply does not seem feasible from a practical standpoint. One might consider using a higher order numerical integration or curve-fitting technique. However, no curve-fitting method will capture regions undefined by the available points, such as leading-edge suction regions, or, as in this case, the sting shroud. The remainder of this report describes an alternative method for correcting the integrated pressure results without increasing the number of pressure taps.

The pressure integration used a discrete pressure and a discrete normal vector for each panel. As the number of integration panels increases, the integration method more accurately approximates the effects of a continuous pressure field. The difference between the force computed from the discretized integration method and that from a continuous pressure field acting on infinitesimal areas is defined to be the discretization error.

Figure 18 compares the size of the densest computational grid to the experimental integration panels at one location on the model. Since the FLO57 surface grid is so dense, it was assumed to approximate the continuous pressure field encountered in the real world. The discretization error was then quantified in the following manner:

1. The pressure FLO57 predicted at each tap location was found. Grid and tap locations generally did not correspond, so tap pressures were obtained by interpolating from the surrounding cell centers to the tap.
2. These interpolated pressures were combined with the experimental tap areas and unit normals, and were then integrated in the same manner as the experimental pressures.
3. Drag polars from step 2 and from the original FLO57 solution were then plotted together. The difference between these curves, shown in figure 19, quantifies the discretization error.

Therefore, by relying entirely upon the computational solution, an estimate for the discretization error experienced by the experimental pressure-integration scheme can be determined. Because FLO57 provides an accurate estimation of the surface pressures, the discretization error found in figure 19 can reasonably be expected to apply to the experimental pressure integration. The results of the experimental pressure integration should improve once this discretization error is removed from the integration. The experimental pressure integration with the discretization error removed is shown in figure 20. After the skin friction estimate is added to this curve, it almost directly overlays the balance data.

It is important to note here that the discretization error described above also includes the effect of the sting shroud discussed in the previous section, because the FLO57 results were obtained using geometry that had the shroud included. Therefore, this error estimation method is also capable of capturing geometric differences between the integration geometry and the actual model configuration.

Unfortunately, the method does not retain the same accuracy for all test conditions. At Mach = 0.40, as shown in figure 21, the discretization error found from FLO57 at high lifts does not match the increment needed to correct the experimental integration. However, at lower angles of attack the correction works very well.

The deviation at high angles of attack is most likely due to the computational solution failing to model the flow field accurately at those test conditions. An examination of the FLO57 results at Mach = 0.40 reveals that the computational drag polars demonstrate a greater increase in induced drag than do the experimental data. When the discretization error determined from this computational solution at Mach = 0.40 is removed from the experimental pressure integration as in figure 21, the final result also demonstrates too large an increase in drag due to lift. However, the zero-lift drag coefficient matches the balance data almost exactly. Therefore, in estimating the discretization error with a computational solution by the method just described, it is necessary to limit it to conditions where the flow field is accurately modeled by the CFD code.

The discretization error found from the computations is essentially the integration error due to the inability to interpolate pressures accurately between taps. The success of this method results from using the computational solution in place of a "higher-order" integrator. In addition, since the computational geometry was not limited by the sting shroud, the integrated experimental pressure data were easily corrected for that as well.

## CONCLUSION

The Euler-based flow solver, FLO57, has been compared extensively with experimental data at three Mach numbers and several angles of attack. The code accurately predicted surface pressure distributions over the forward regions of the model, but it demonstrated limited performance downstream because of its inviscid assumptions.

In addition, the flow solution was used to improve the results of an experimental study with the objective of determining the feasibility of using experimentally measured pressures to obtain absolute values of forces and moments acting on a wind tunnel model. By using the computational solution to correct for the discretization error caused by a finite number of pressure taps, accurate values for drag were obtained.

Experimentation and CFD can be used for the mutual benefit of both. Proper experimental validation of CFD codes is necessary to determine the conditions under which computations may be expected to give satisfactory results. In addition, CFD solutions may be used to assist the experimenter before a test by improving the conceptual design, by indicating locations of large pressure gradients for improved pressure tap placement, and by projecting the test-condition limitations due to balance design limits. Furthermore, as demonstrated in this study, CFD may be used after a test to improve the quality and resolution of the experimental data.

## REFERENCES

- Carmichael, R. L.; and Erickson, L. L.: PANAIR – A Higher Order Panel Method for Predicting Subsonic or Supersonic Linear Potential Flows About Arbitrary Configurations. AIAA Paper 81-1255, June 1981.
- Enomoto, F.; and Keller, P.: Using a Commercial CAD System for Simultaneous Input to Theoretical Aerodynamic Programs and Wind-Tunnel Model Construction. NASA CP-2272, 1983.
- Goodsell, A.; Madson, M.; and Melton, J.: TranAir and Euler Computations of a Generic Fighter Including Comparisons with Experimental Data. AIAA Paper 89-0263, January 1989.
- Hermstad, D. L.: RAID User's Guide, Technical Note No. 33, Rev. 2, Sterling Federal Systems, Inc., Palo Alto, CA, 1989.
- Jameson, A.; and Baker, T. J.: Solution of the Euler Equations for Complex Configurations. AIAA Paper 83-1929CP, in AIAA Computational Fluid Dynamics Conference proceedings, 1983.
- Newsome, R. W.; and Kandil, O. A.: Vortical Flow Aerodynamics – Physical Aspects and Numerical Simulation. AIAA Paper 87-0205, January 1987.
- Rice, J. R.: Numerical Methods, Software, and Analysis: IMSL<sup>®</sup> Reference Edition. McGraw-Hill, Inc., 1983, pp. 186-215.
- Schlichting, Hermann: Boundary-Layer Theory. McGraw-Hill, Inc., 1979, pp. 140 and 640.
- Sivells, James C.; and Payne, Robert G.: A Method of Calculating Turbulent-Boundary-Layer Growth at Hypersonic Mach Numbers. AEDC-TR-59-3, ASTIA Doc. No. AD-208774, Arnold Eng. Dev. Center, MA, 1959.

TABLE 1. Grid Information and Memory Requirements for FLO57

Grid	i dim	j dim	k dim	Surface Points	Total Points	Memory MW	CPU sec/case
Coarse	67	21	43	45×43	60,501	2	3100
Medium	89	29	57	57×57	147,117	4	7800
Fine	113	37	73	73×73	305,213	8	18000

TABLE 2. CFD Solutions

Mach	$\alpha$	Coarse	Medium	Fine	PANAIR
0.4	-4,-2,0,2,4,6,8,10	X	X		X
0.7	-4,-2,0,2,4,6,8,10	X	X		X
0.8	-4,-2,0,2,4,6,8,10	X	X	X	X

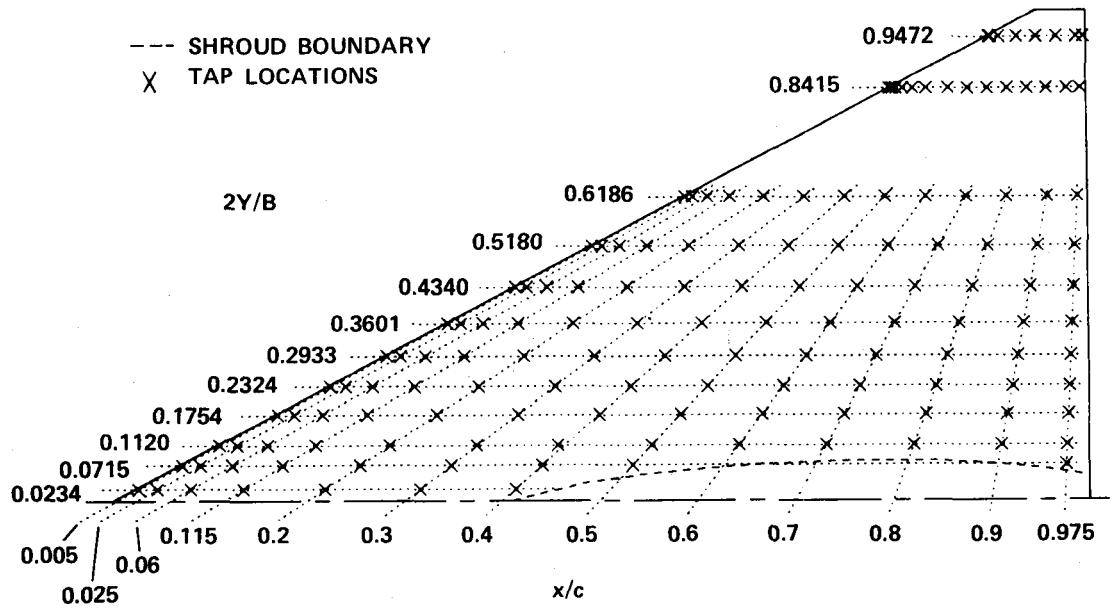


Figure 1.—Upper surface plan view showing pressure tap locations.

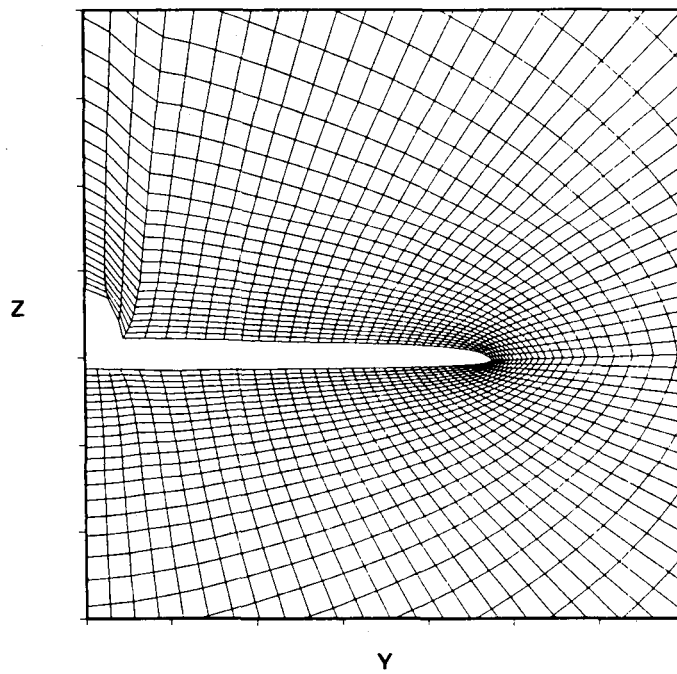


Figure 2.—Typical grid plane near trailing edge.

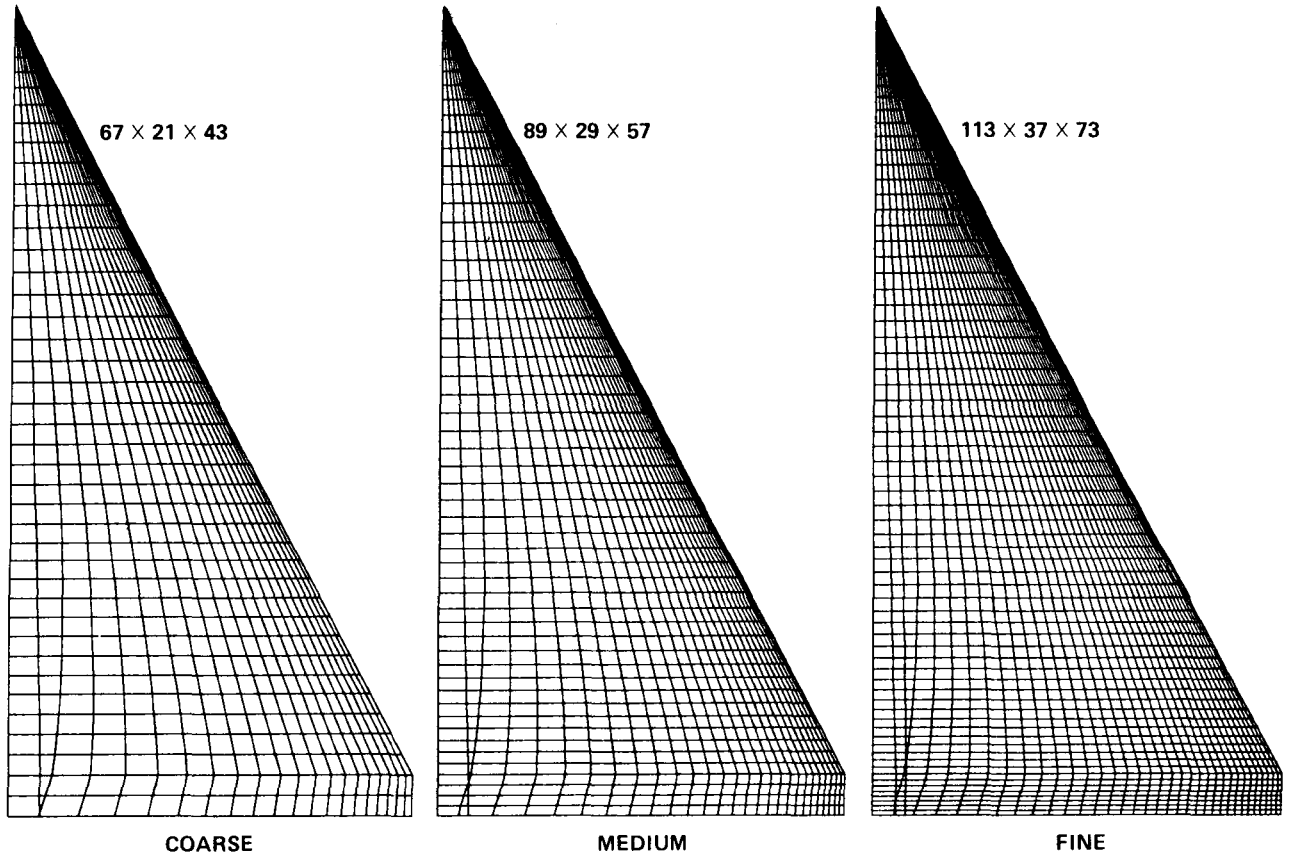


Figure 3.—Surface grid distributions for FLO57 analysis.

	MACH	$\alpha$	$C_L$	$C_D$	$C_M$
— FLO57 MEDIUM	0.401	-4.05	-0.1046	0.0048	-0.0014
- - - FLO57 COARSE	0.401	-4.05	-0.1069	0.0059	-0.0012
○ WIND TUNNEL	0.401	-4.05	-0.0999	0.0115	-0.0007

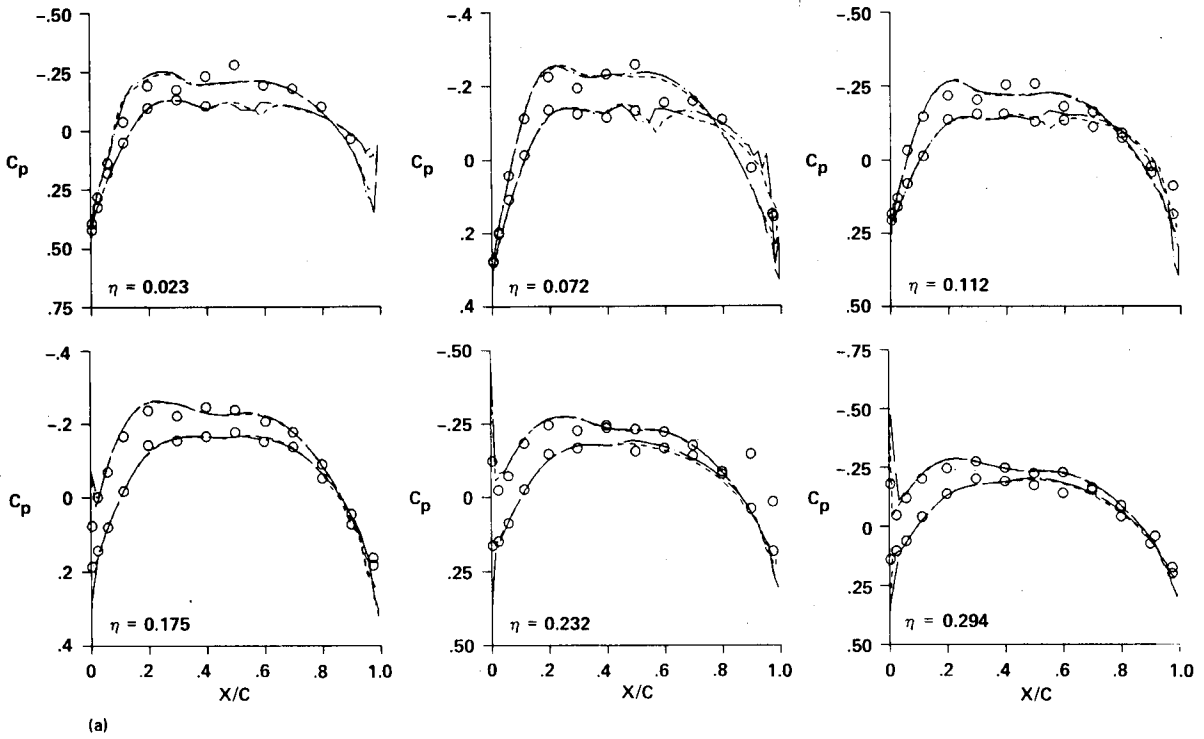


Figure 4.—Inboard/outboard sectional  $C_p$  distributions for  $M = 0.4$ .

	MACH	$\alpha$	$C_L$	$C_D$	$C_M$
— FLO57 MEDIUM	0.401	-4.05	-0.1046	0.0048	-0.0014
- - - FLO57 COARSE	0.401	-4.05	-0.1069	0.0059	-0.0012
○ WIND TUNNEL	0.401	-4.05	-0.0999	0.0115	-0.0007

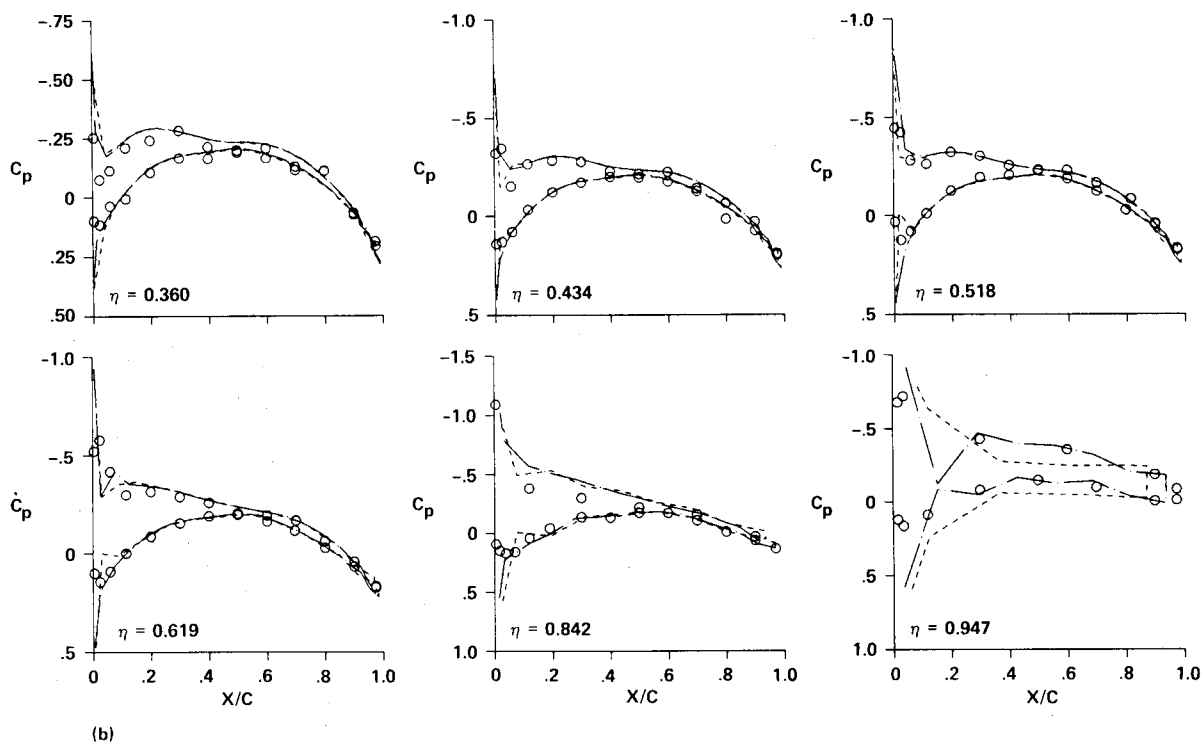


Figure 4.-Continued.

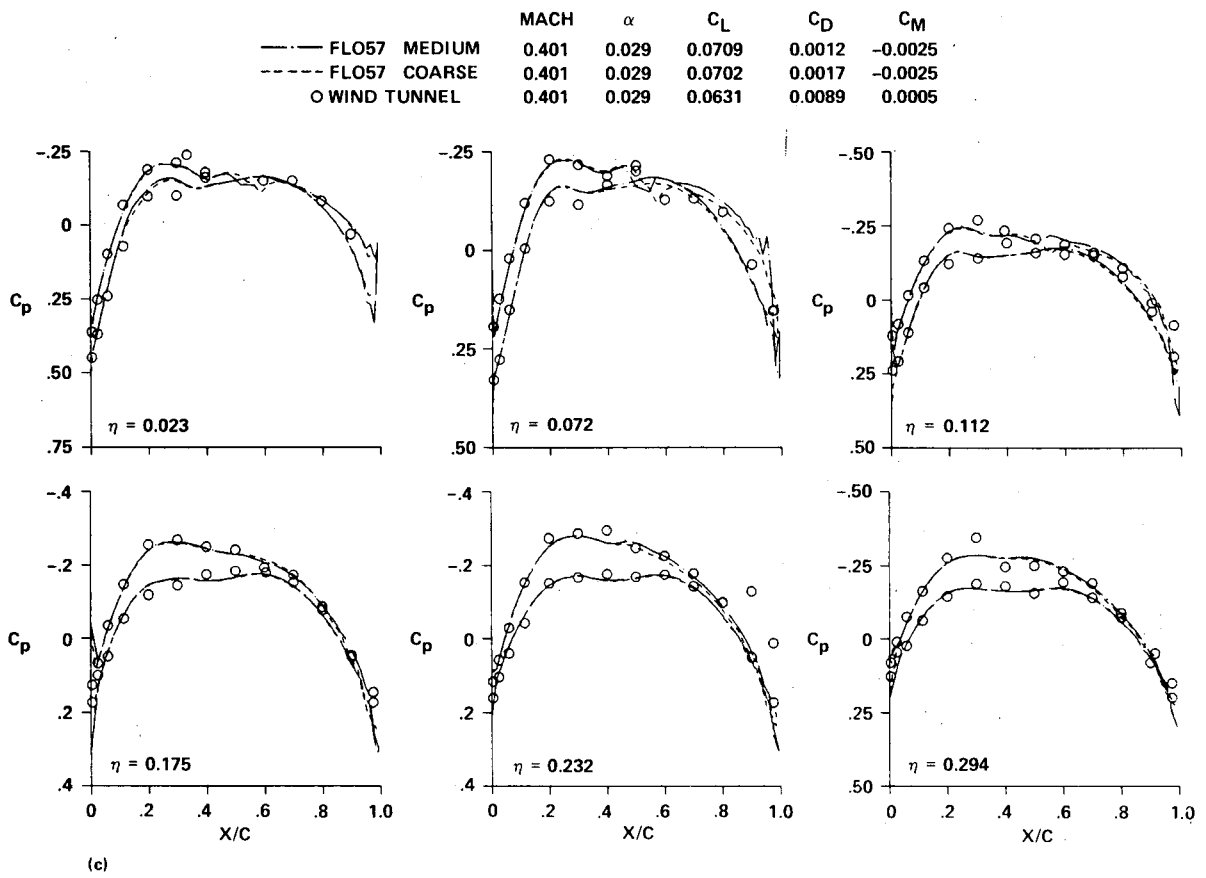
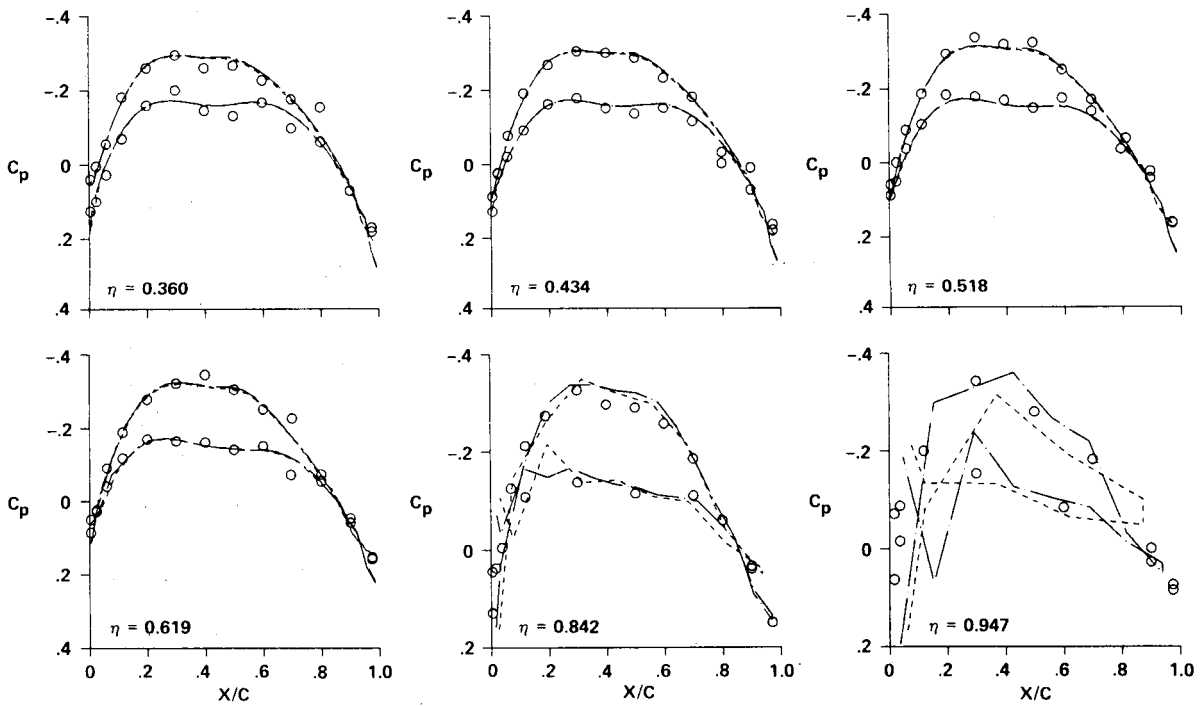


Figure 4.—Continued.

	MACH	$\alpha$	$C_L$	$C_D$	$C_M$
— FLO57 MEDIUM	0.401	0.029	0.0709	0.0012	-0.0025
- - - FLO57 COARSE	0.401	0.029	0.0702	0.0017	-0.0025
○ WIND TUNNEL	0.401	0.029	0.0631	0.0089	0.0005



(d)

Figure 4.—Continued.

	MACH	$\alpha$	$C_L$	$C_D$	$C_M$
— FLO57 MEDIUM	0.400	3.964	0.2358	0.0123	-0.0029
- - - FLO57 COARSE	0.400	3.964	0.2368	0.0132	-0.0028
○ WIND TUNNEL	0.400	3.964	0.2162	0.0175	0.0025

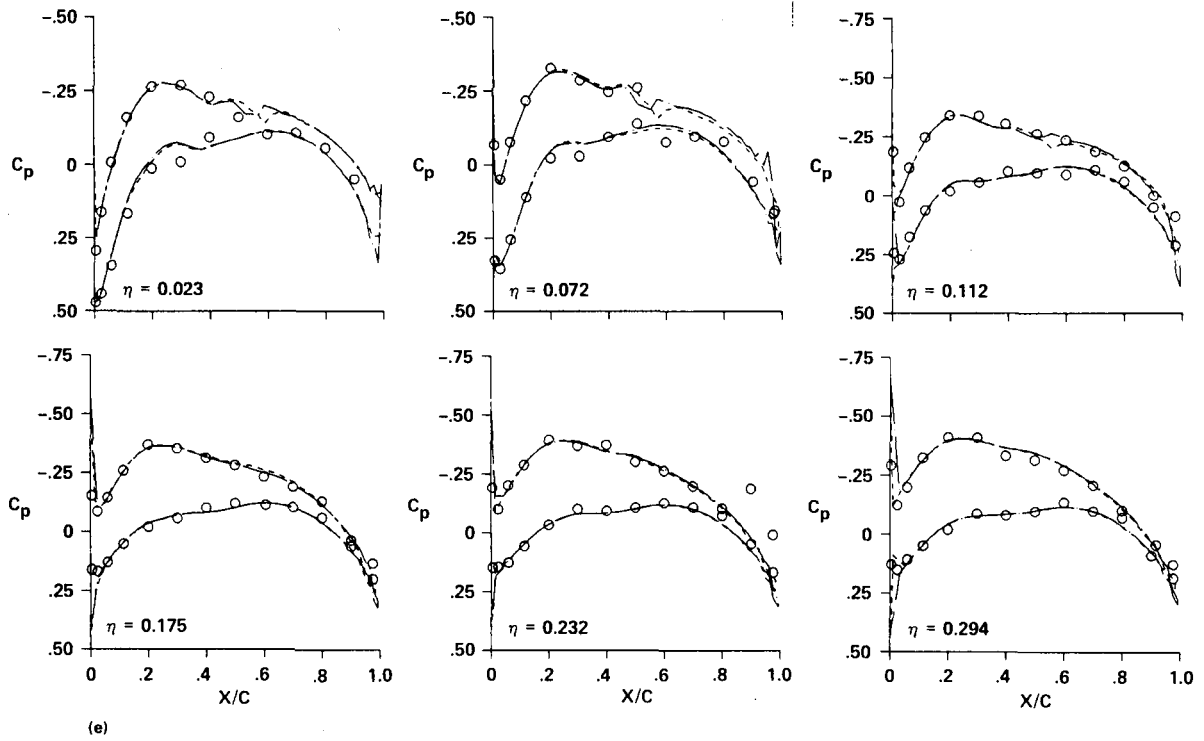
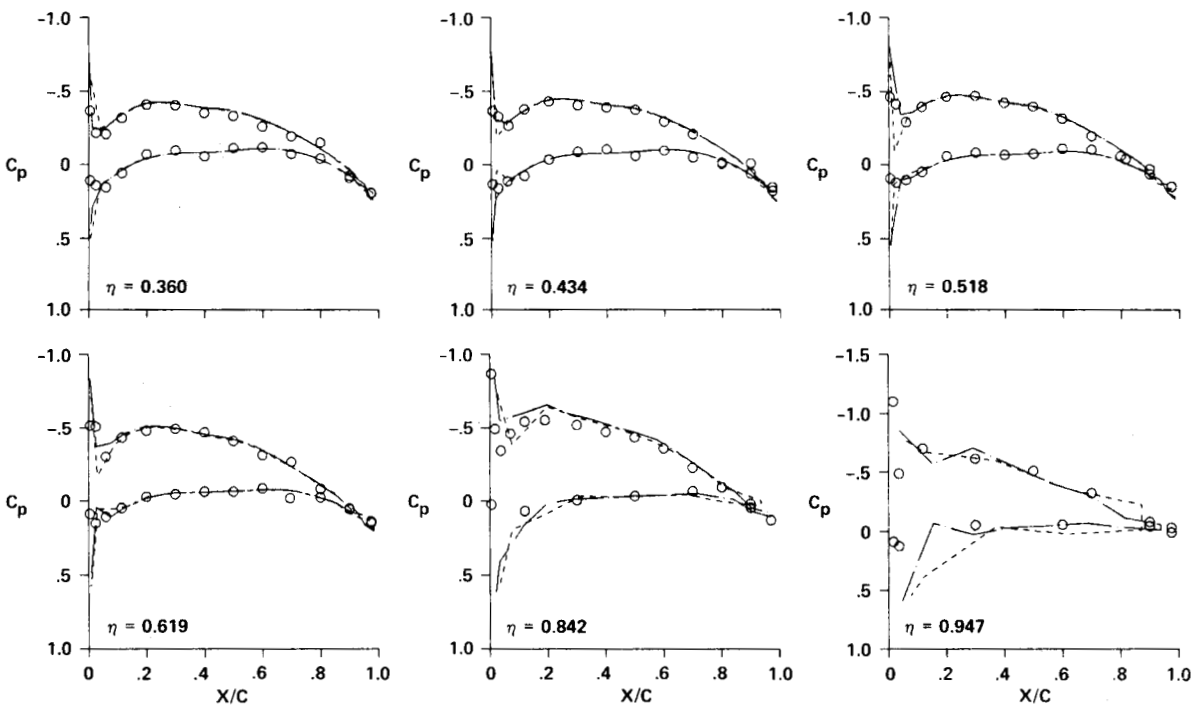


Figure 4.—Continued.

	MACH	$\alpha$	$C_L$	$C_D$	$C_M$
— FLO57 MEDIUM	0.400	3.964	0.2358	0.0123	-0.0029
- - - FLO57 COARSE	0.400	3.964	0.2368	0.0132	-0.0028
○ WIND TUNNEL	0.400	3.964	0.2162	0.0175	0.0025



(f)

Figure 4.—Continued.

	MACH	$\alpha$	$C_L$	$C_D$	$C_M$
— FLO57 MEDIUM	0.399	8.008	0.4209	0.0451	-0.0039
- - - FLO57 COARSE	0.399	8.008	0.4170	0.0473	-0.0028
○ WIND TUNNEL	0.399	8.008	0.3921	0.0441	0.0032

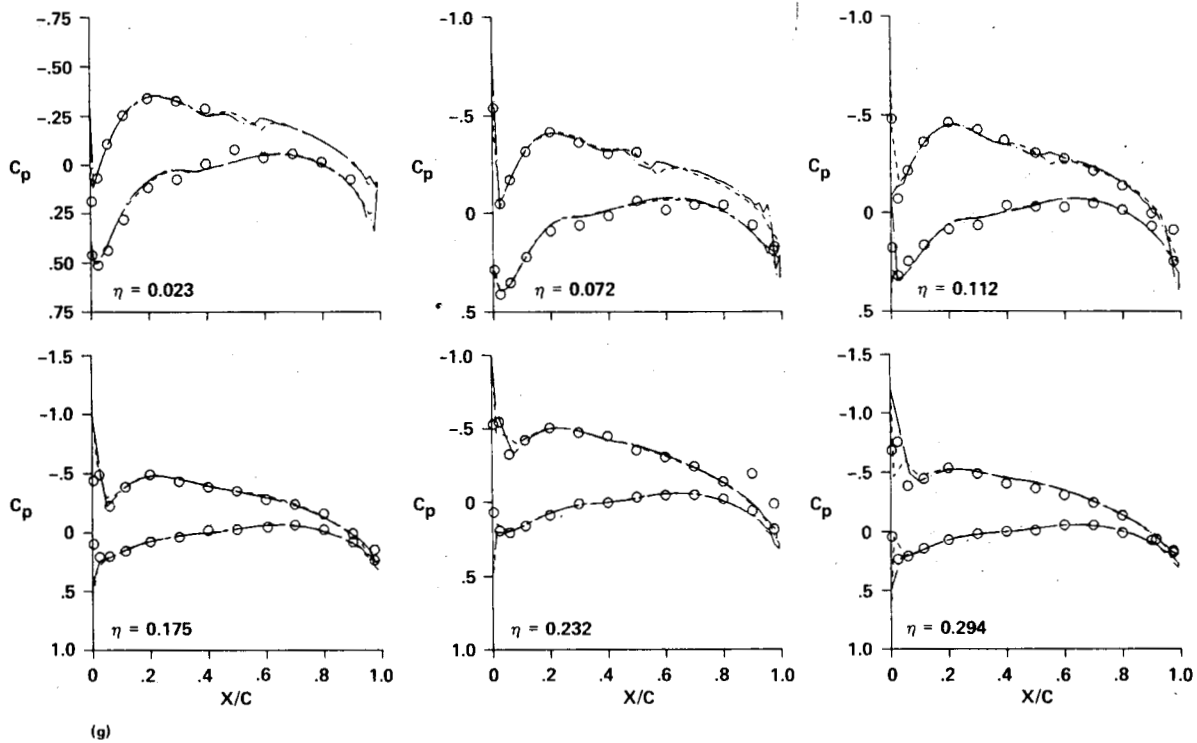


Figure 4.—Continued.

	MACH	$\alpha$	$C_L$	$C_D$	$C_M$
— FLO57 MEDIUM	0.399	8.008	0.4209	0.0451	-0.0039
- - - FLO57 COARSE	0.399	8.008	0.4170	0.0473	-0.0028
○ WIND TUNNEL	0.399	8.008	0.3921	0.0441	0.0032

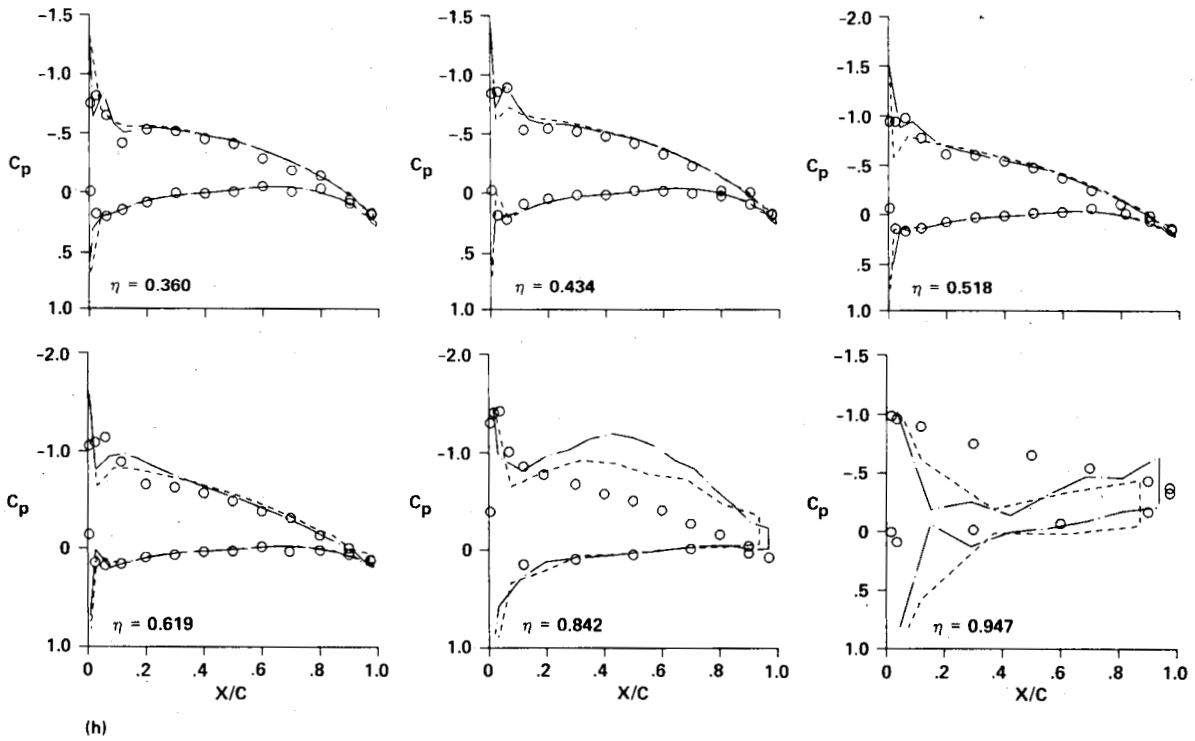


Figure 4.—Concluded.

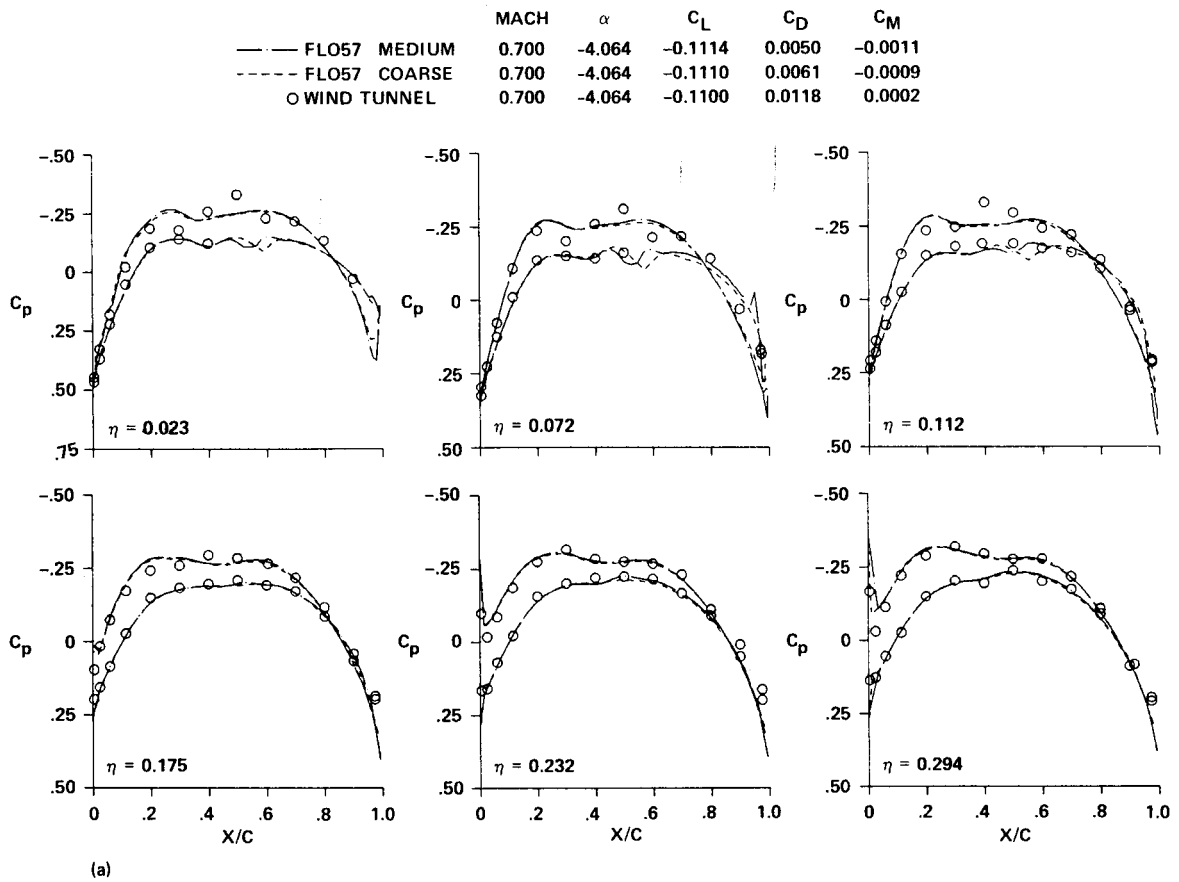


Figure 5.—Inboard/outboard sectional  $C_p$  distributions for  $M = 0.7$ .

	MACH	$\alpha$	$C_L$	$C_D$	$C_M$
— FLO57 MEDIUM	0.700	-4.064	-0.1114	0.0050	-0.0011
- - - FLO57 COARSE	0.700	-4.064	-0.1110	0.0061	-0.0009
○ WIND TUNNEL	0.700	-4.064	-0.1100	0.0118	0.0002

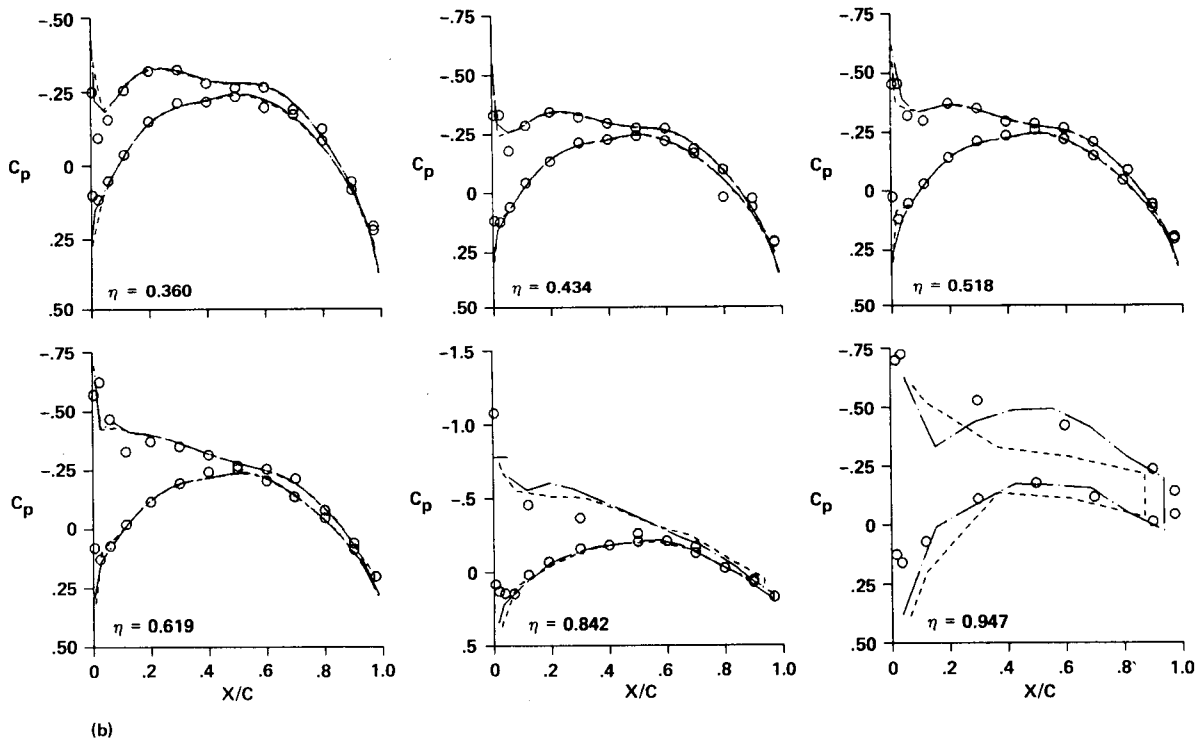


Figure 5.—Continued.

	MACH	$\alpha$	$C_L$	$C_D$	$C_M$
— FLO57 MEDIUM	0.700	0.155	0.0838	0.0014	-0.0042
- - - FLO57 COARSE	0.700	0.155	0.0815	0.0020	-0.0039
○ WIND TUNNEL	0.700	0.155	0.0661	0.0090	0.0006

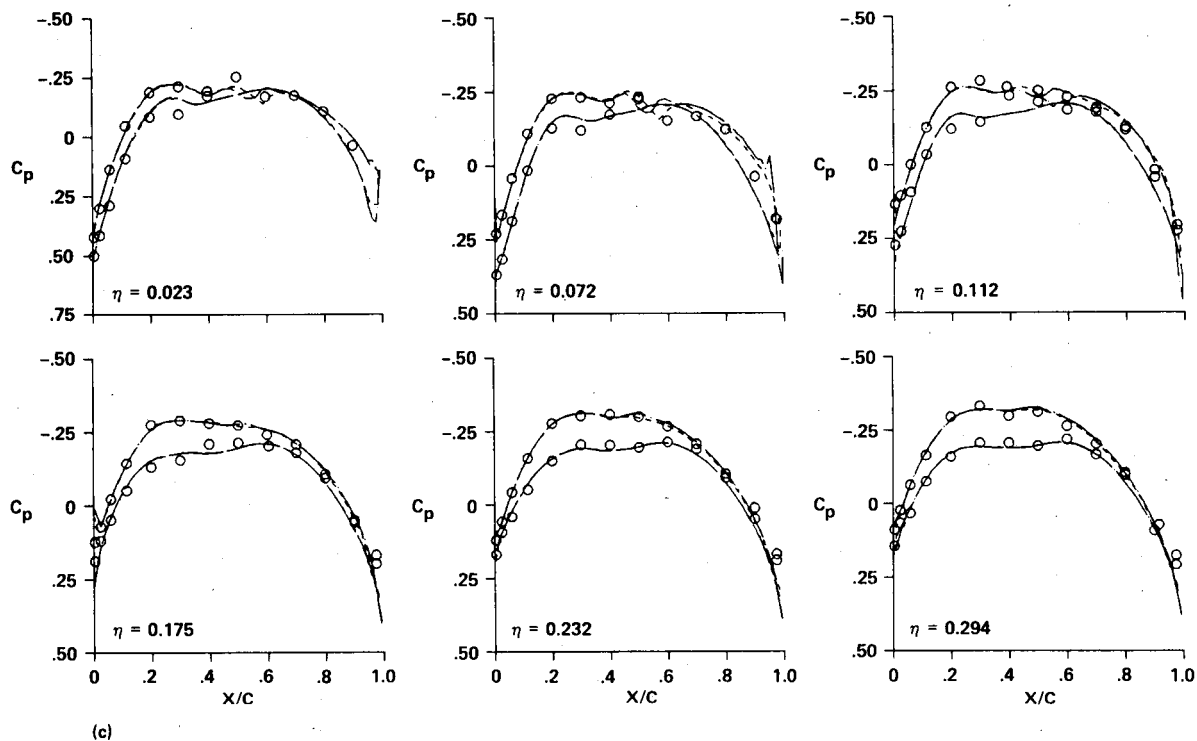


Figure 5.—Continued.

	MACH	$\alpha$	$C_L$	$C_D$	$C_M$
— FLO57 MEDIUM	0.700	0.155	0.0838	0.0014	-0.0042
- - - FLO57 COARSE	0.700	0.155	0.0815	0.0020	-0.0039
○ WIND TUNNEL	0.700	0.155	0.0661	0.0090	0.0005

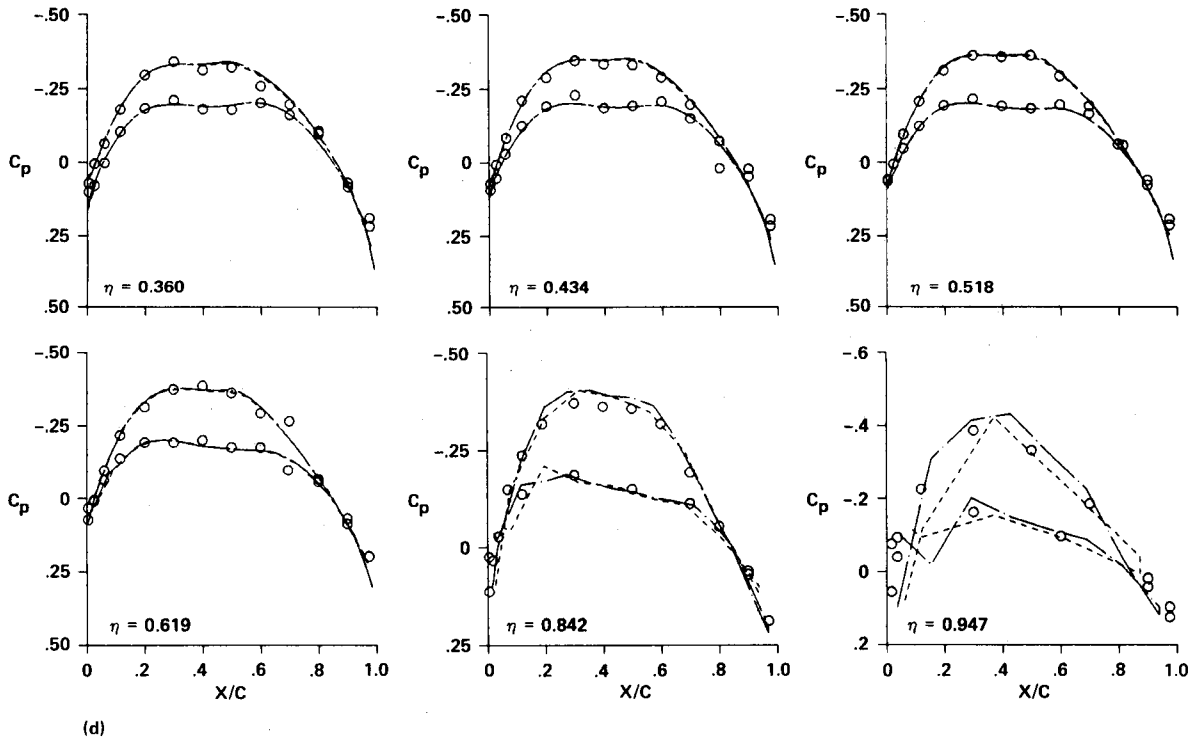


Figure 5.—Continued.

	MACH	$\alpha$	$C_L$	$C_D$	$C_M$
— FLO57 MEDIUM	0.699	4.322	0.2681	0.0160	-0.0050
- - - FLO57 COARSE	0.699	4.332	0.2672	0.0171	-0.0049
○ WIND TUNNEL	0.699	4.322	0.2391	0.0201	0.0030

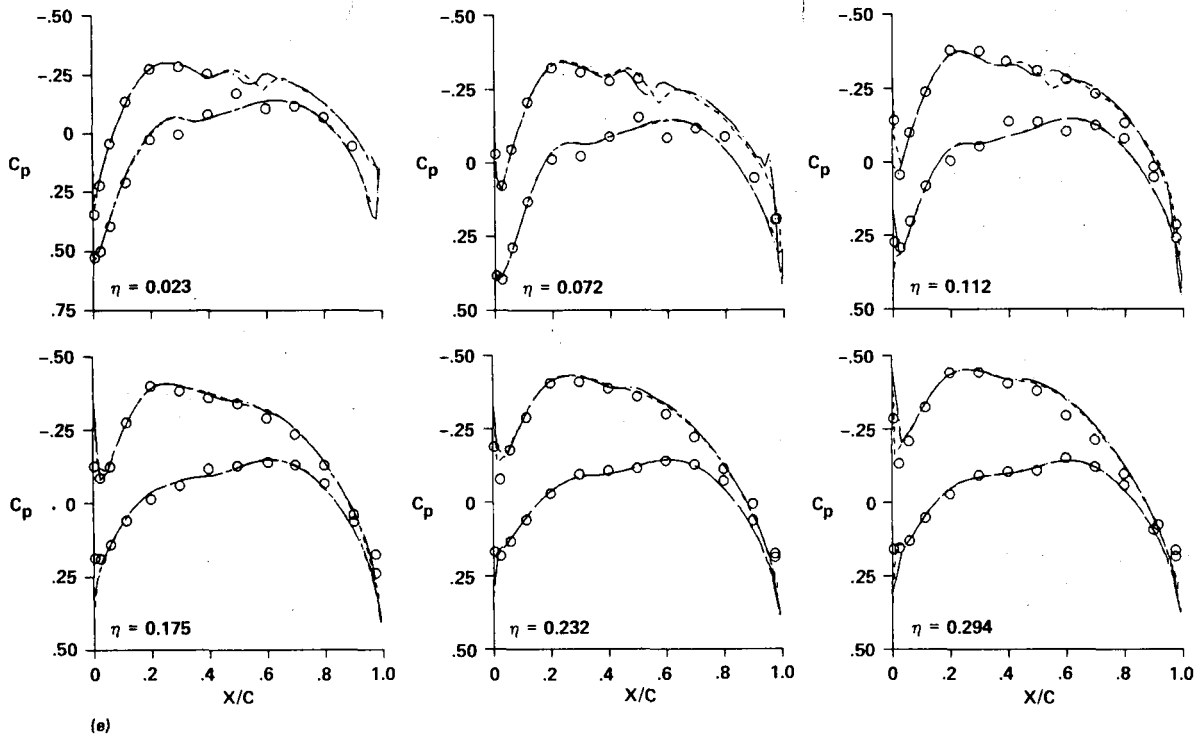


Figure 5.—Continued.

	MACH	$\alpha$	$C_L$	$C_D$	$C_M$
— FLO57 MEDIUM	0.699	4.322	0.2681	0.0160	-0.0050
- - - FLO57 COARSE	0.699	4.322	0.2672	0.0171	-0.0049
○ WIND TUNNEL	0.699	4.322	0.2391	0.0201	0.0030

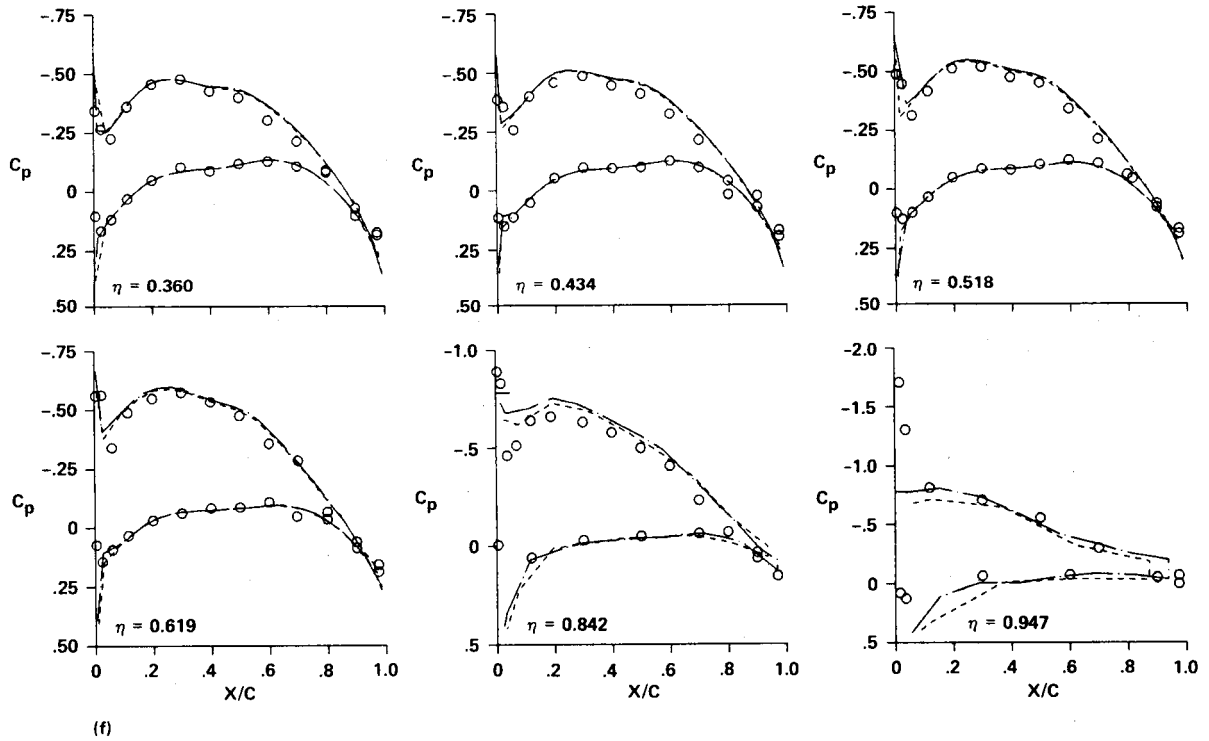


Figure 5.—Continued.

	MACH	$\alpha$	$C_L$	$C_D$	$C_M$
— FLO57 MEDIUM	0.701	8.531	0.4652	0.0565	-0.0039
- - - FLO57 COARSE	0.701	8.531	0.4735	0.0610	-0.0082
○ WIND TUNNEL	0.701	8.531	0.4249	0.0540	0.0047

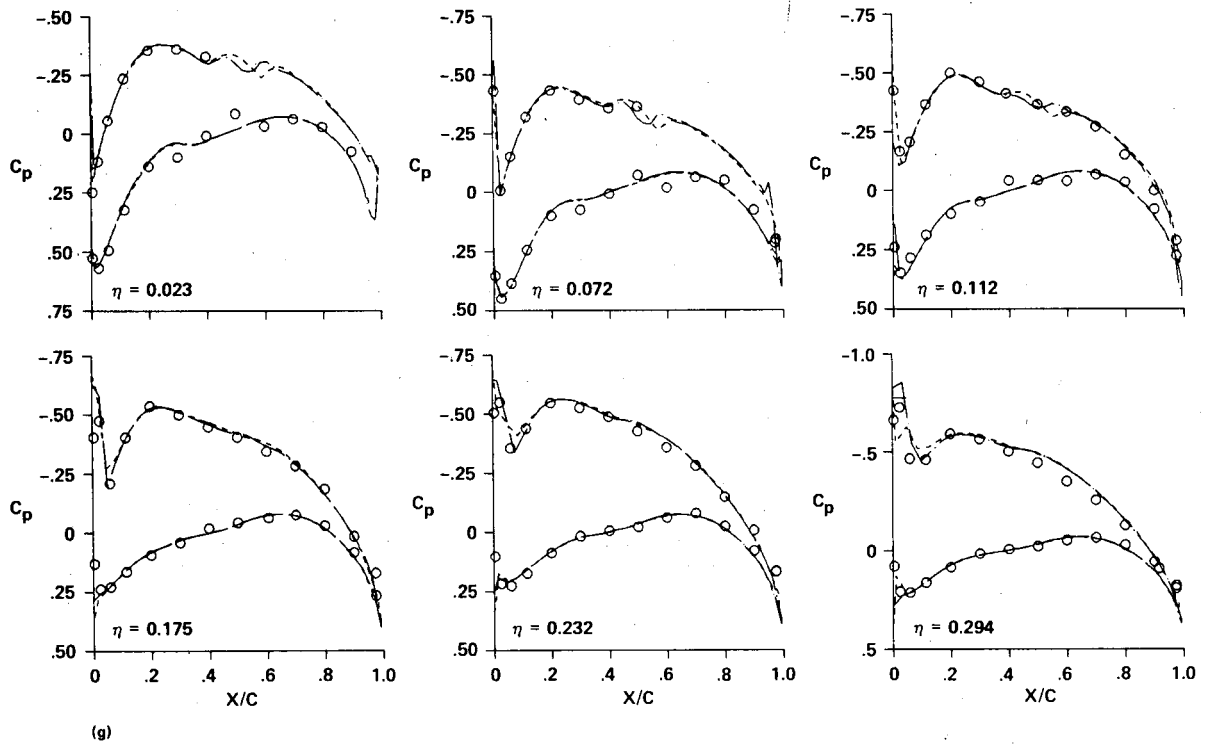


Figure 5.—Continued.

	MACH	$\alpha$	$C_L$	$C_D$	$C_M$
— FLO57 MEDIUM	0.701	8.531	0.4652	0.0565	-0.0039
- - - FLO57 COARSE	0.701	8.531	0.4735	0.0610	-0.0082
○ WIND TUNNEL	0.701	8.531	0.4249	0.0540	0.0047

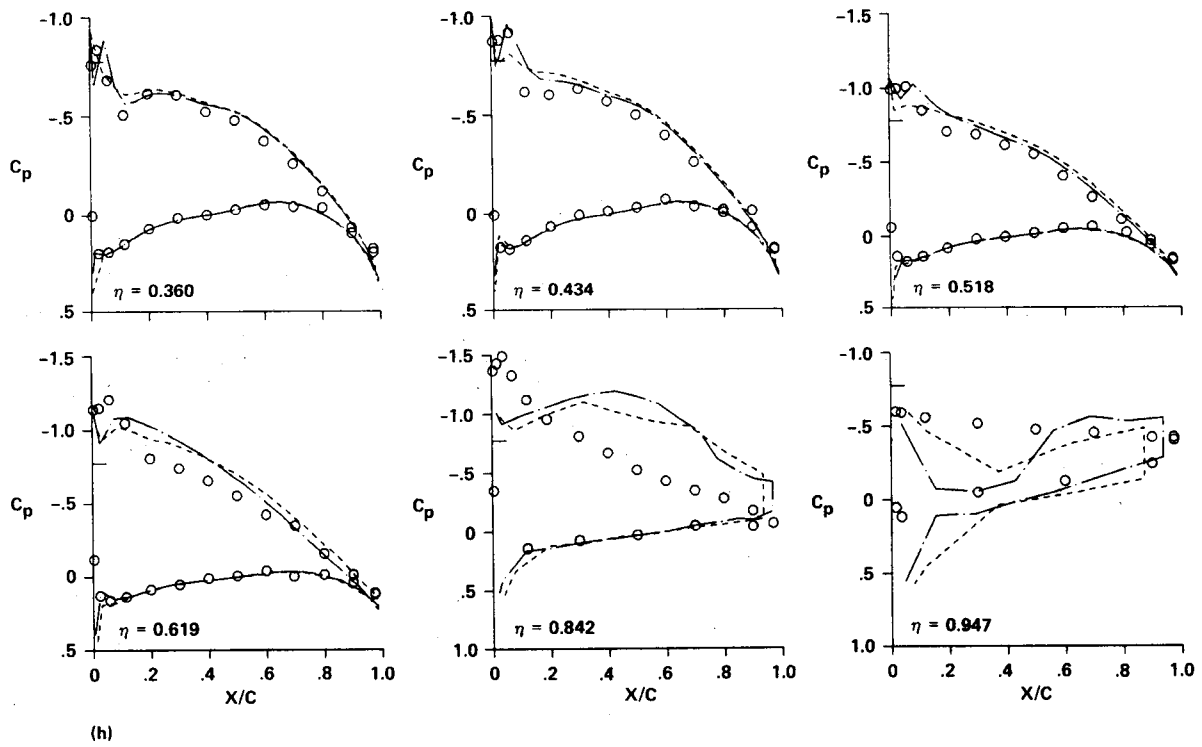


Figure 5.—Concluded.

	MACH	$\alpha$	$C_L$	$C_D$	$C_M$
— FLO57 FINE	0.800	0.000	0.0771	0.0008	-0.0043
- - - FLO57 MEDIUM	0.800	0.000	0.0809	0.0011	-0.0053
⋯ FLO57 COARSE	0.800	0.000	0.0784	0.0020	-0.0049
× PANAIR	0.800	-0.120	0.0751	0.0007	-0.0047
○ WIND TUNNEL	0.801	0.399	0.0773	0.0099	0.0018

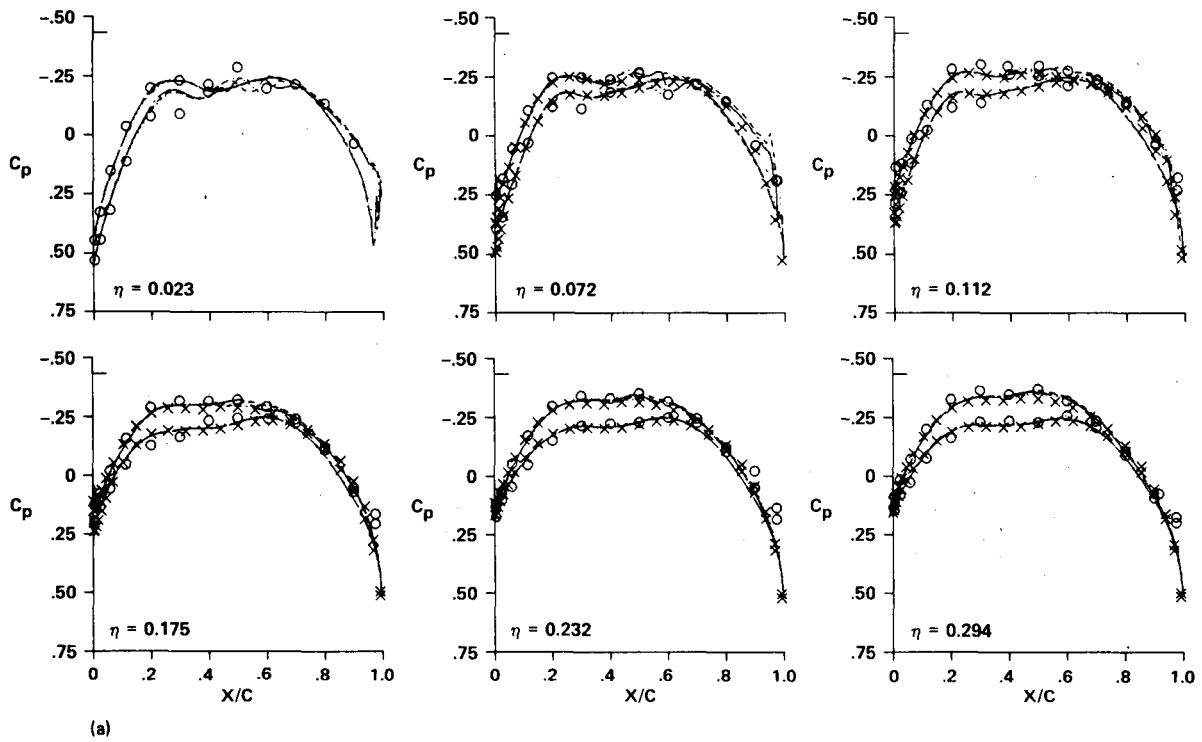


Figure 6.—Inboard/outboard sectional  $C_p$  distributions for  $M = 0.8$ .

	MACH	$\alpha$	$C_L$	$C_D$	$C_M$
— FLO57 FINE	0.800	0.000	0.0771	0.0008	-0.0043
- - - FLO57 MEDIUM	0.800	0.000	0.0809	0.0011	-0.0053
⋯ FLO57 COARSE	0.800	0.000	0.0784	0.0020	-0.0049
× PANAIR	0.800	-0.120	0.0007	-0.0047	
○ WIND TUNNEL	0.801	0.399	0.0773	0.0099	0.0018

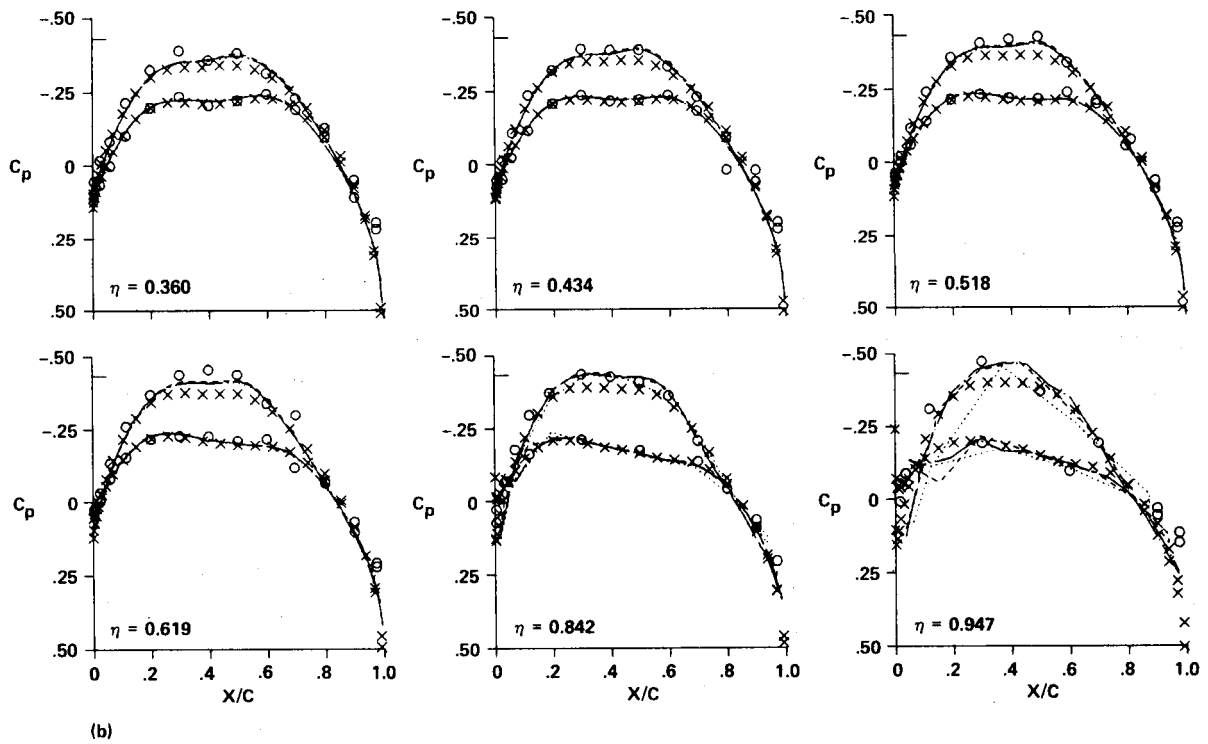


Figure 6.—Continued.

	MACH	$\alpha$	$C_L$	$C_D$	$C_M$
— FLO57 FINE	0.800	4.000	0.2597	0.0145	-0.0051
- - - FLO57 MEDIUM	0.800	4.000	0.2663	0.0153	-0.0073
..... FLO57 COARSE	0.800	4.000	0.2646	0.0167	-0.0072
X PANAIR	0.800	4.110	0.2601	0.0126	-0.0083
O WIND TUNNEL	0.802	4.685	0.2600	0.0230	0.0042

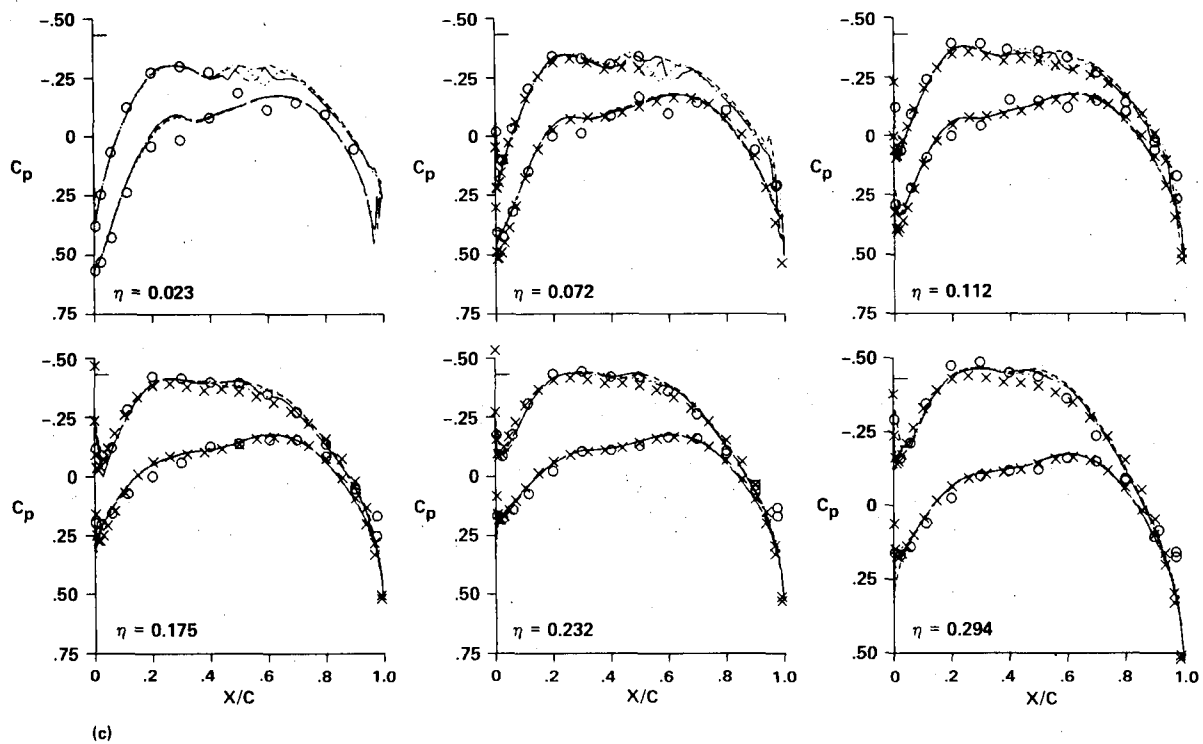


Figure 6.-Continued.

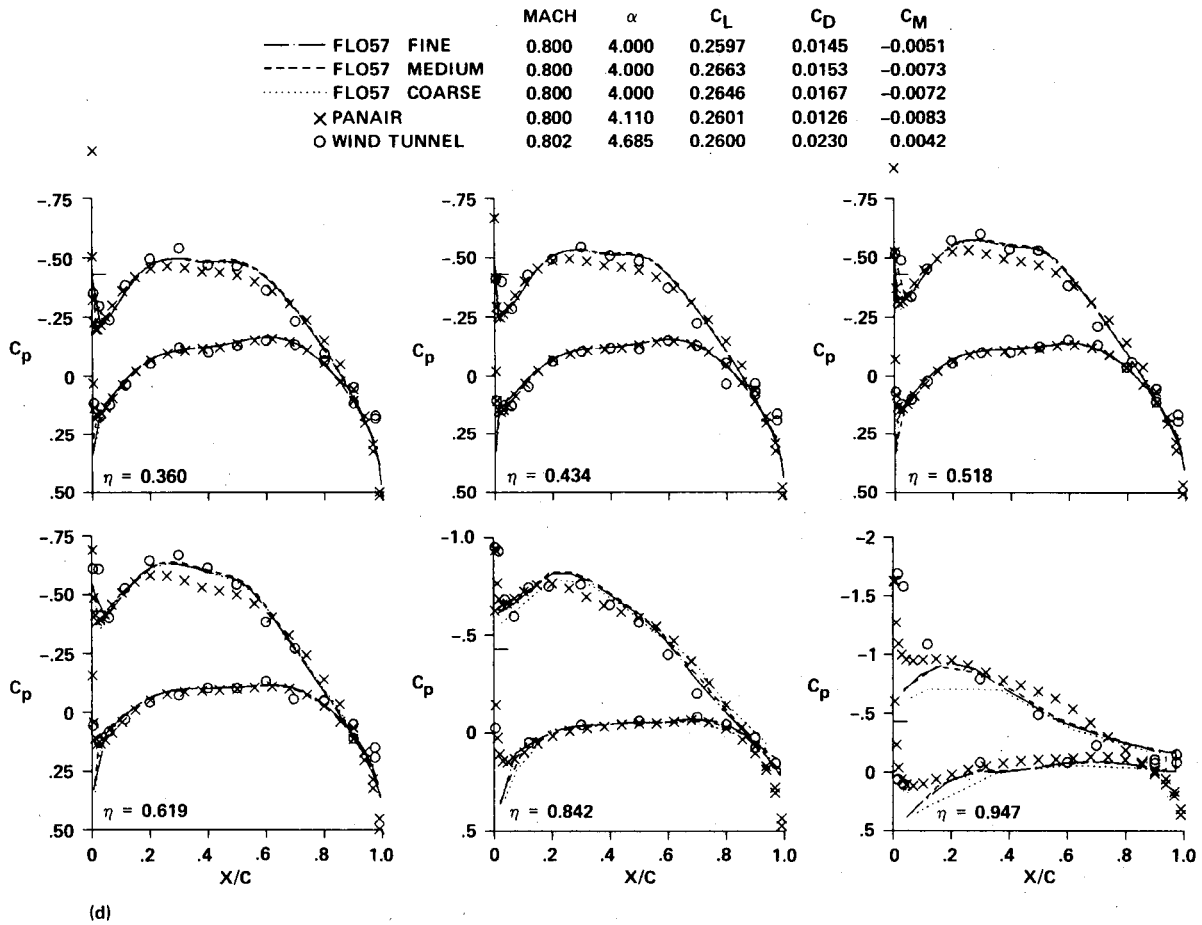


Figure 6.—Continued.

	MACH	$\alpha$	$C_L$	$C_D$	$C_M$
— FLO57 FINE	0.800	7.700	0.4446	0.0504	-0.0079
- - - FLO57 MEDIUM	0.800	7.700	0.4551	0.0529	-0.0122
⋯ FLO57 COARSE	0.800	7.700	0.4475	0.0548	-0.0107
× PANAIR	0.800	8.770	0.0464	-0.0120	
○ WIND TUNNEL	0.801	9.167	0.4600	0.0684	0.0059

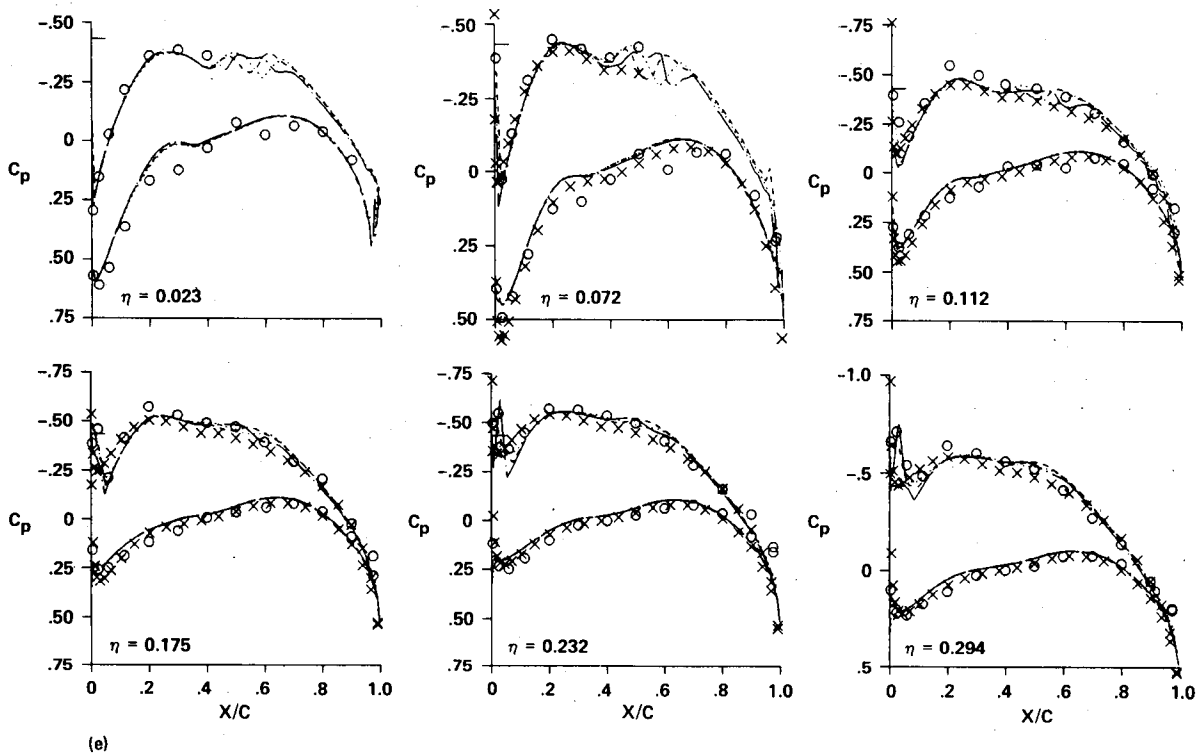


Figure 6.—Continued.

	MACH	$\alpha$	$C_L$	$C_D$	$C_M$
— FLO57 FINE	0.800	7.700	0.4446	0.0504	-0.0079
- - - FLO57 MEDIUM	0.800	7.700	0.4551	0.0529	-0.0122
⋯ FLO57 COARSE	0.800	7.700	0.4475	0.0548	-0.0107
× PANAIR	0.800	8.770	0.4598	0.0464	-0.0120
○ WIND TUNNEL	0.801	9.167	0.4600	0.0684	0.0059

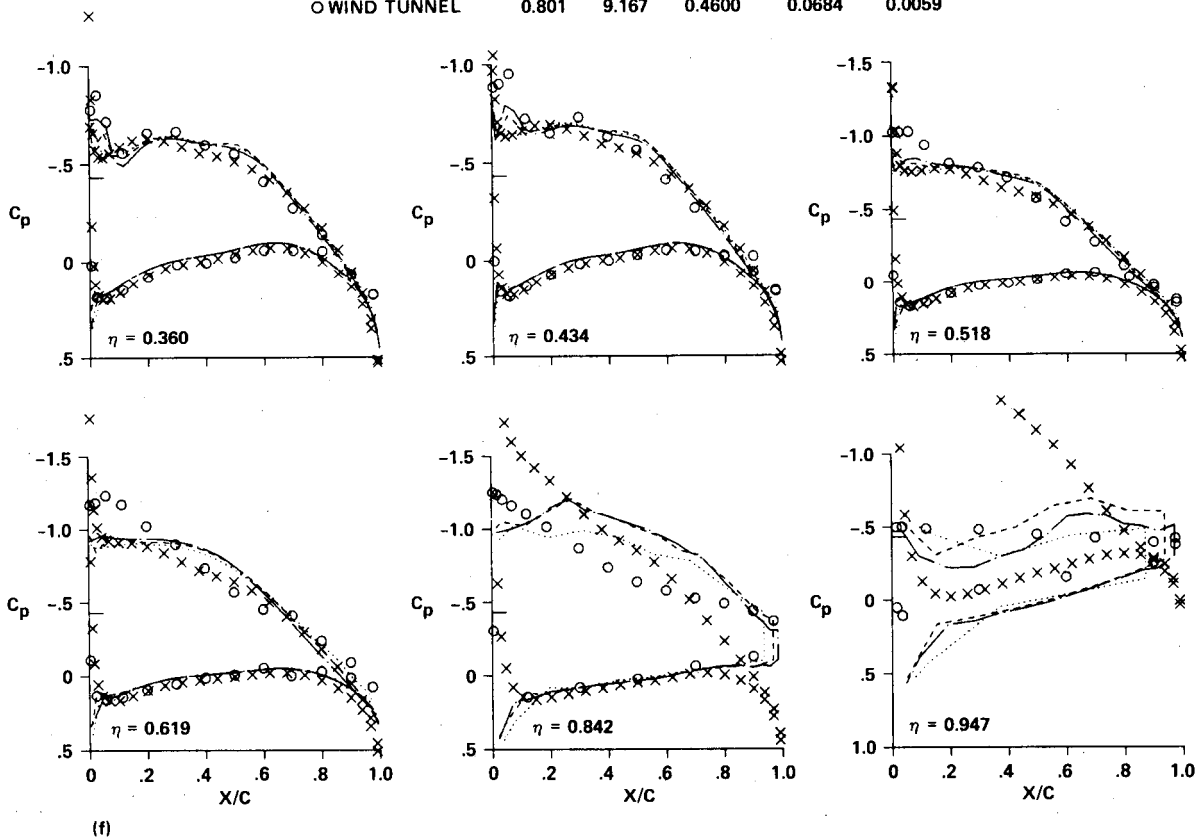


Figure 6.—Concluded.

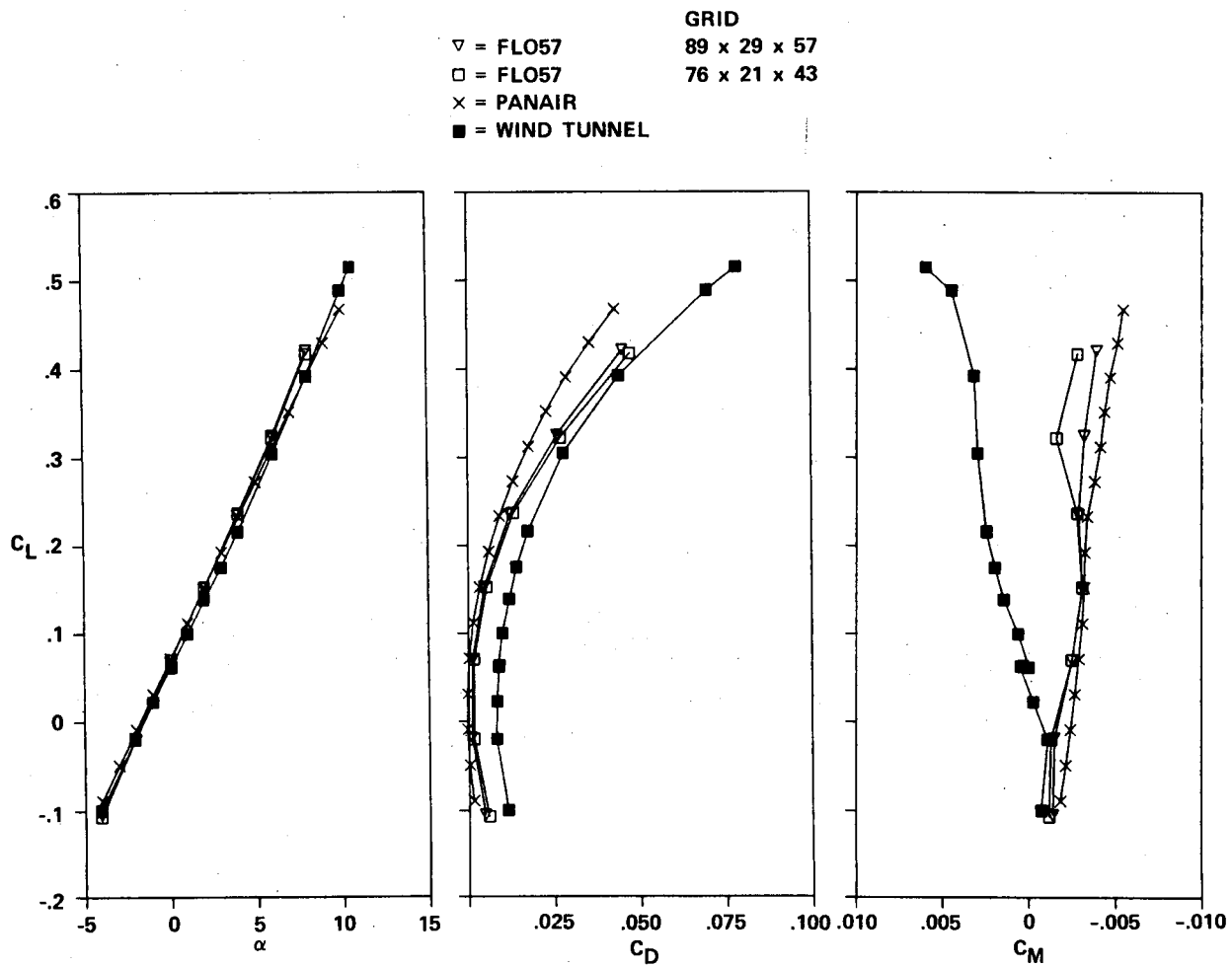


Figure 7.—Lift, drag, and moment data for  $M = 0.4$ .

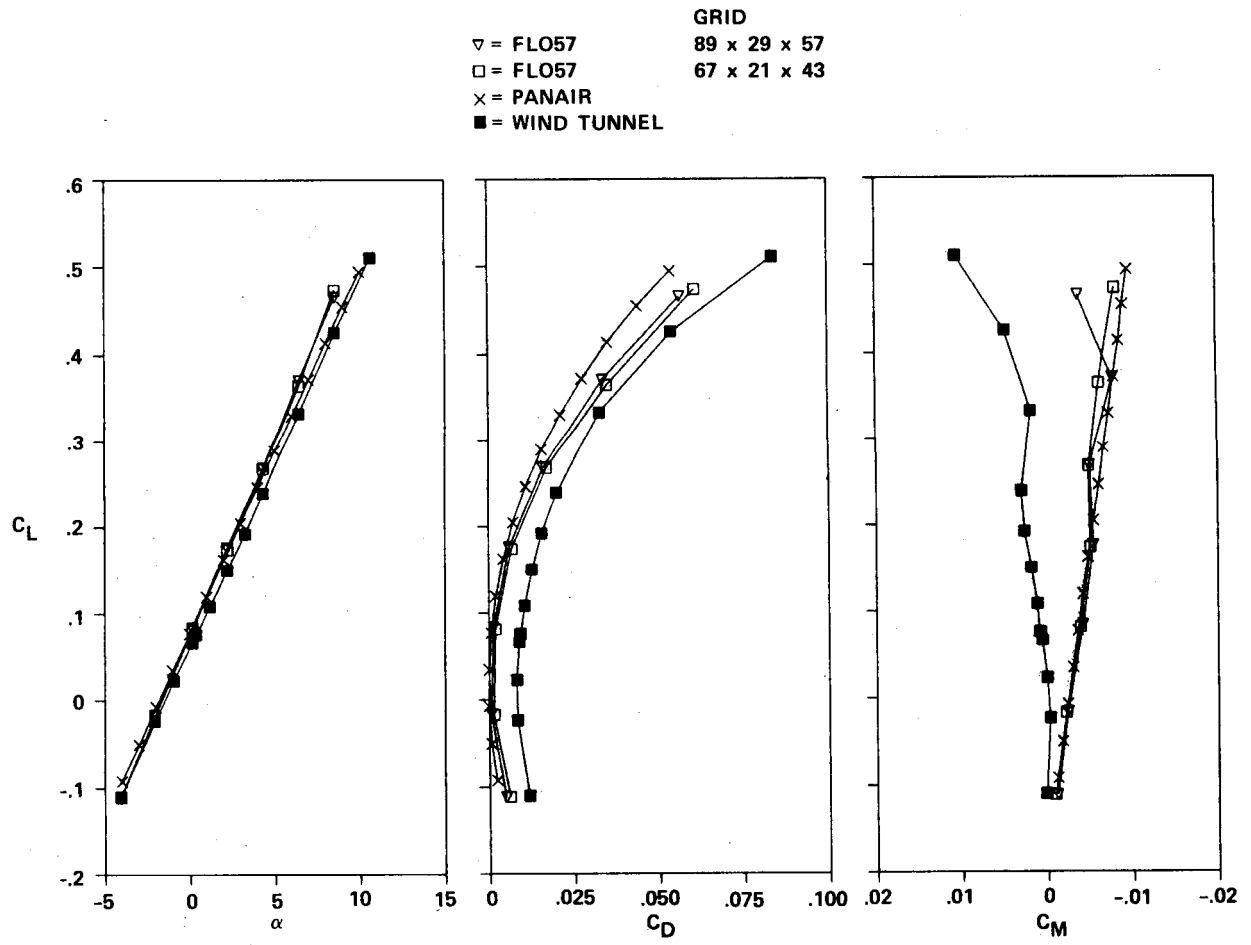


Figure 8.-Lift, drag, and moment data for  $M = 0.7$ .

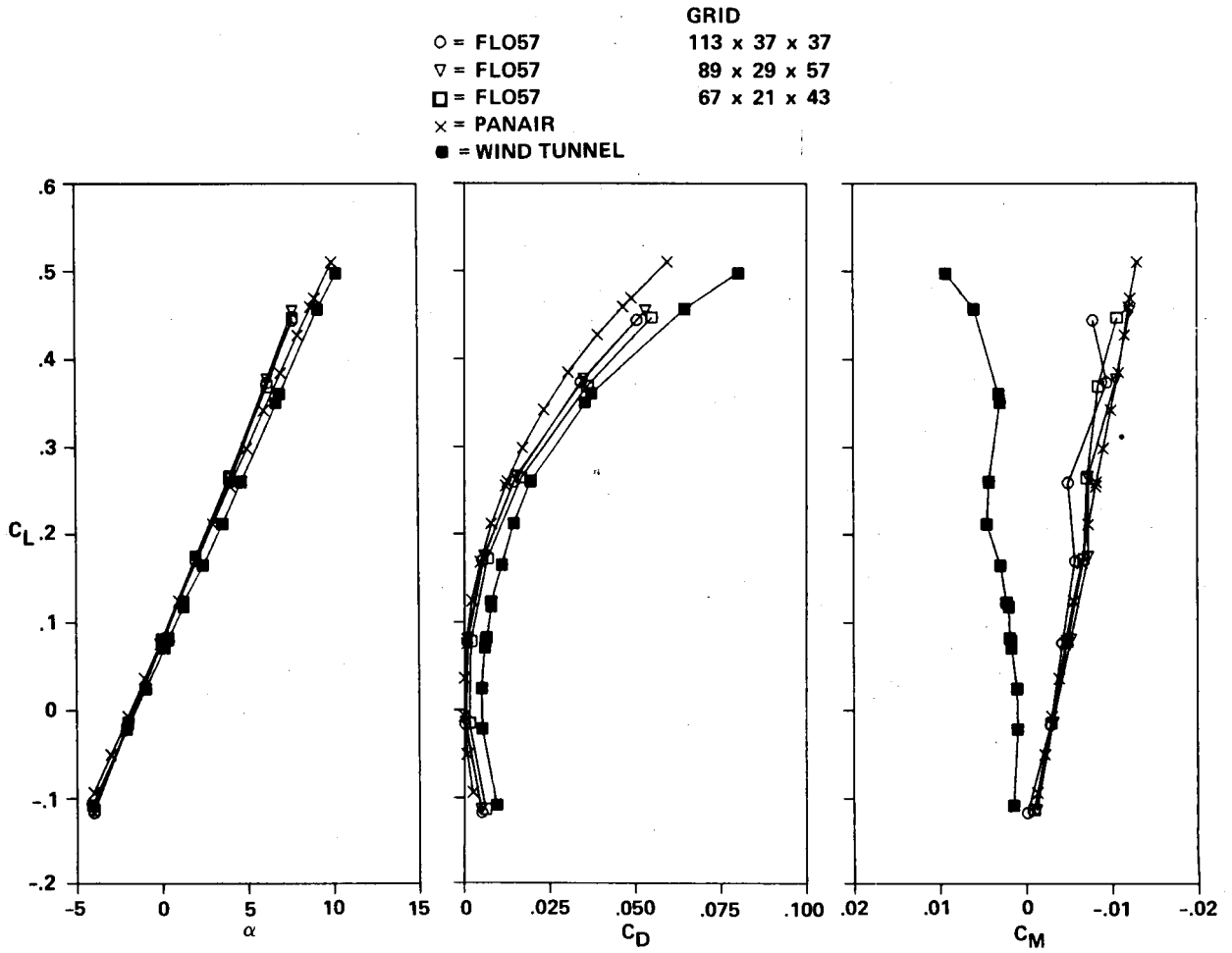
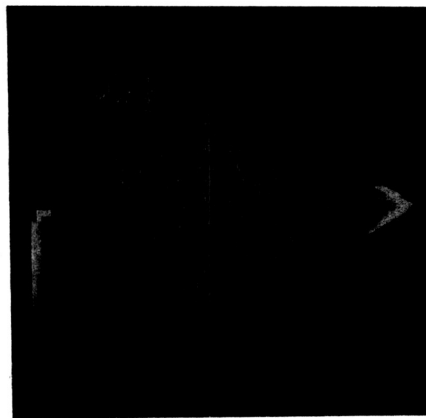
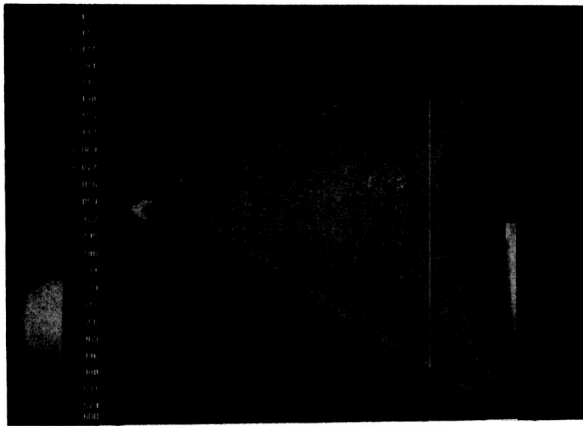
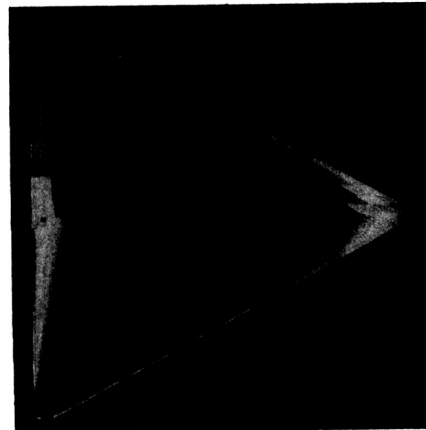
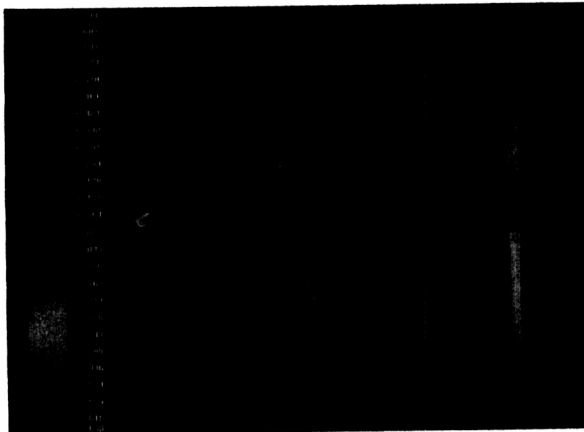


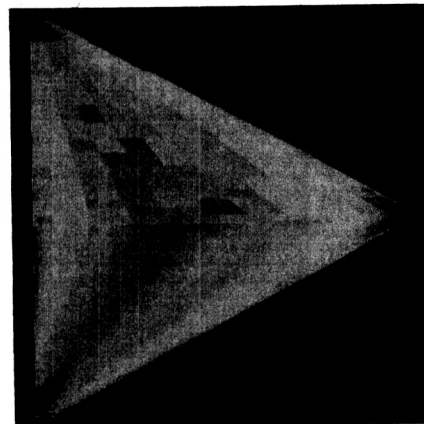
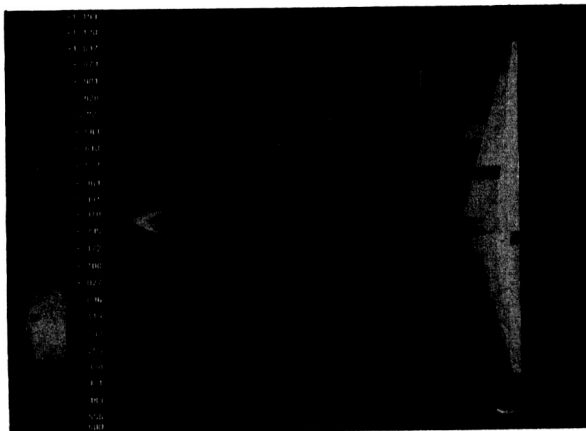
Figure 9.—Lift, drag, and moment data for M = 0.8.



$M = 0.4, \alpha = 0.0293$



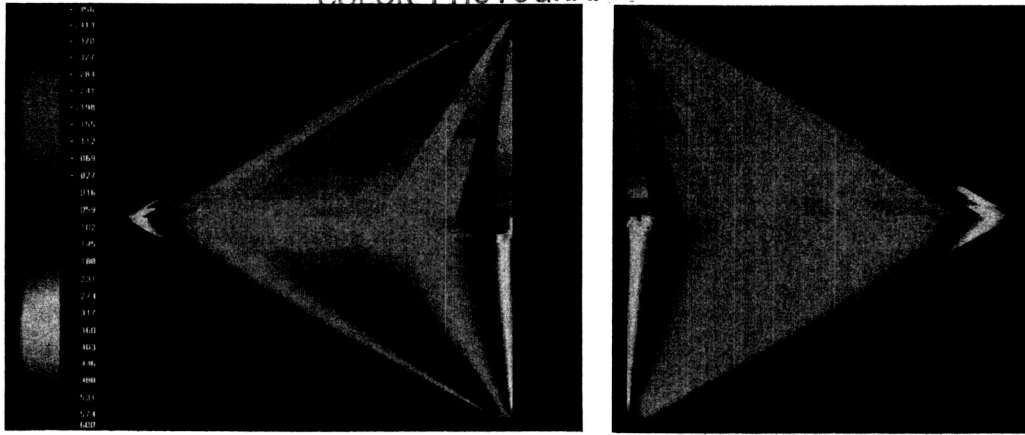
$M = 0.4, \alpha = 3.9641$



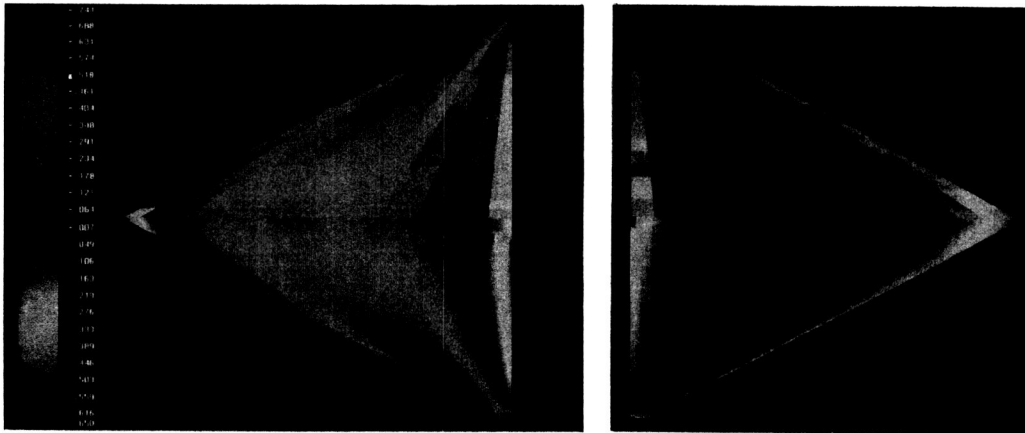
$M = 0.4, \alpha = 8.0081$

Figure 10.-Surface pressure distributions for  $M = 0.4$ .

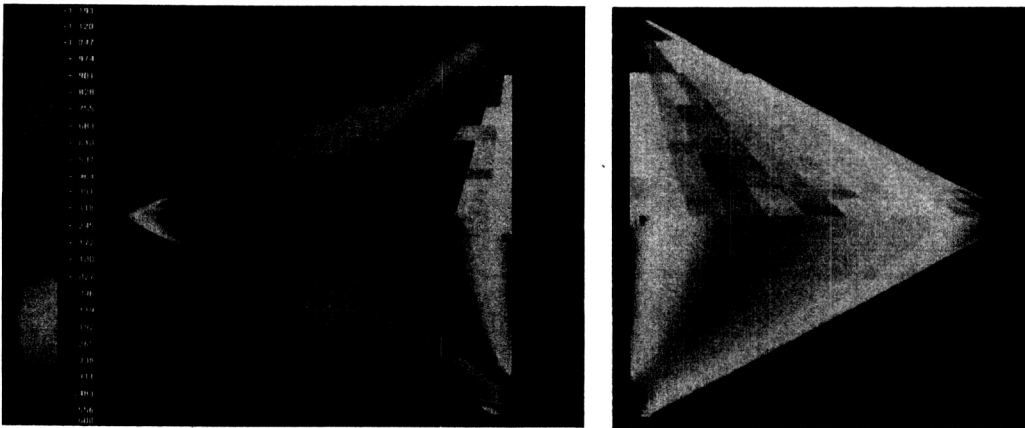
ORIGINAL PAGE  
COLOR PHOTOGRAPH



$M = 0.8, \alpha = 0.399$



$M = 0.8, \alpha = 4.6853$



$M = 0.8, \alpha = 9.1671$

Figure 11.—Surface pressure distributions for  $M = 0.8$ .

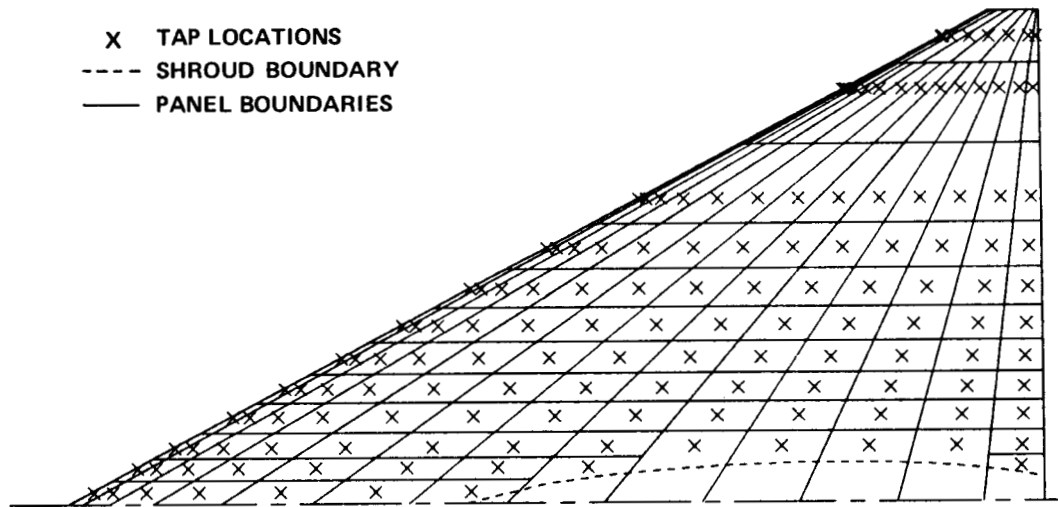


Figure 12.—Tap locations and paneling for experimental pressure integration.

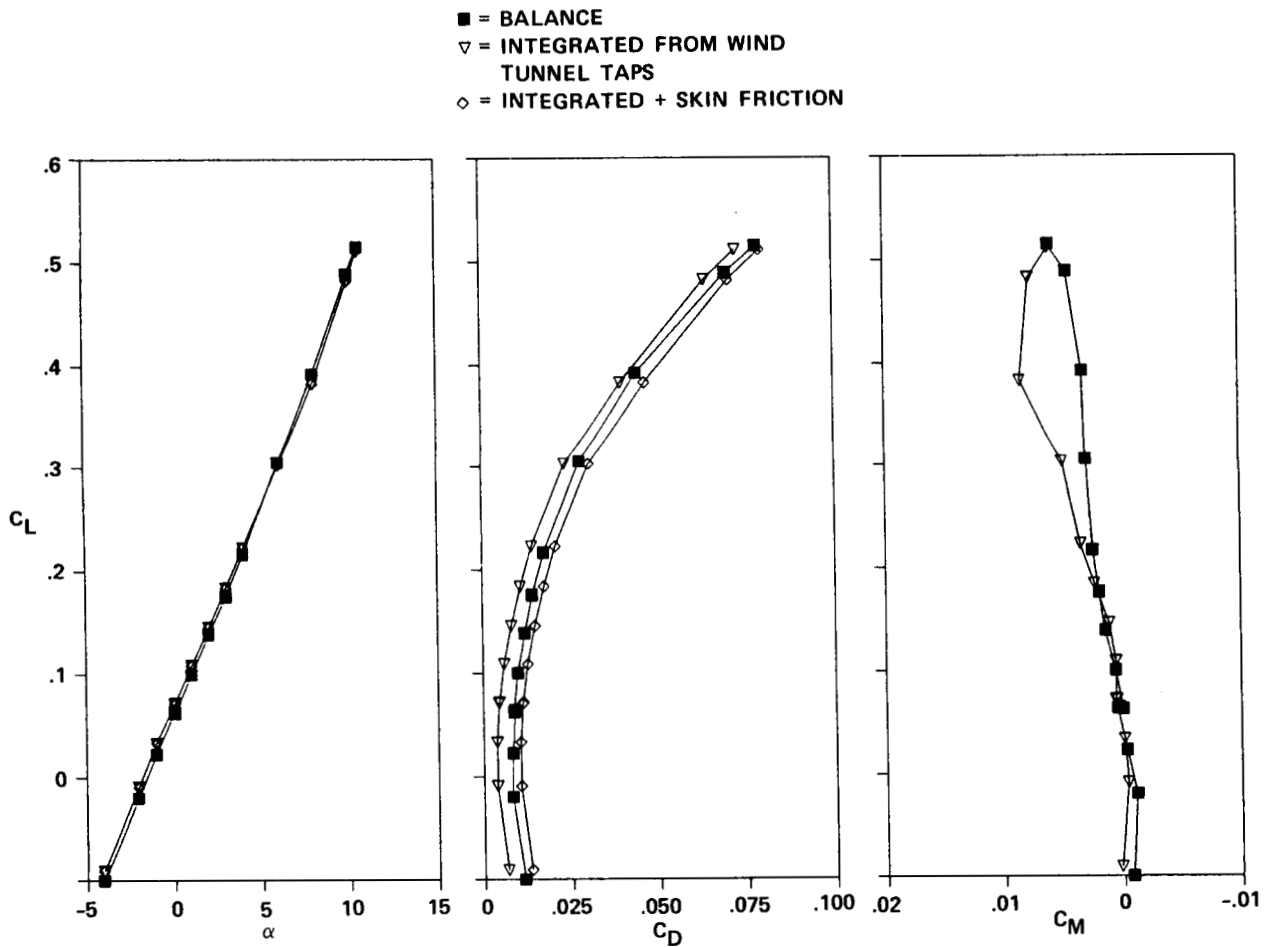


Figure 13.—Lift, drag, and moment data for  $M = 0.4$ .

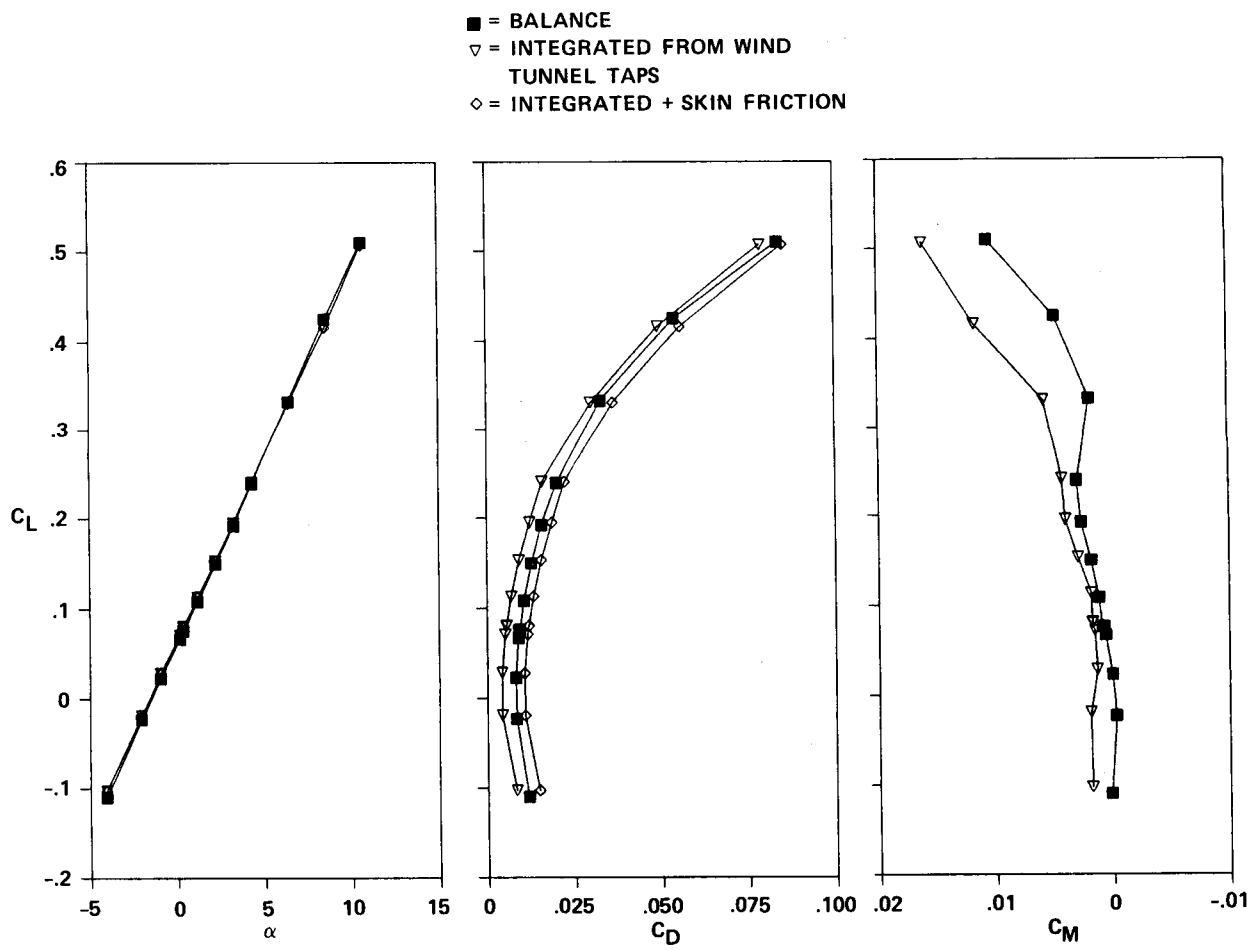


Figure 14.—Lift, drag, and moment data for  $M = 0.7$ .

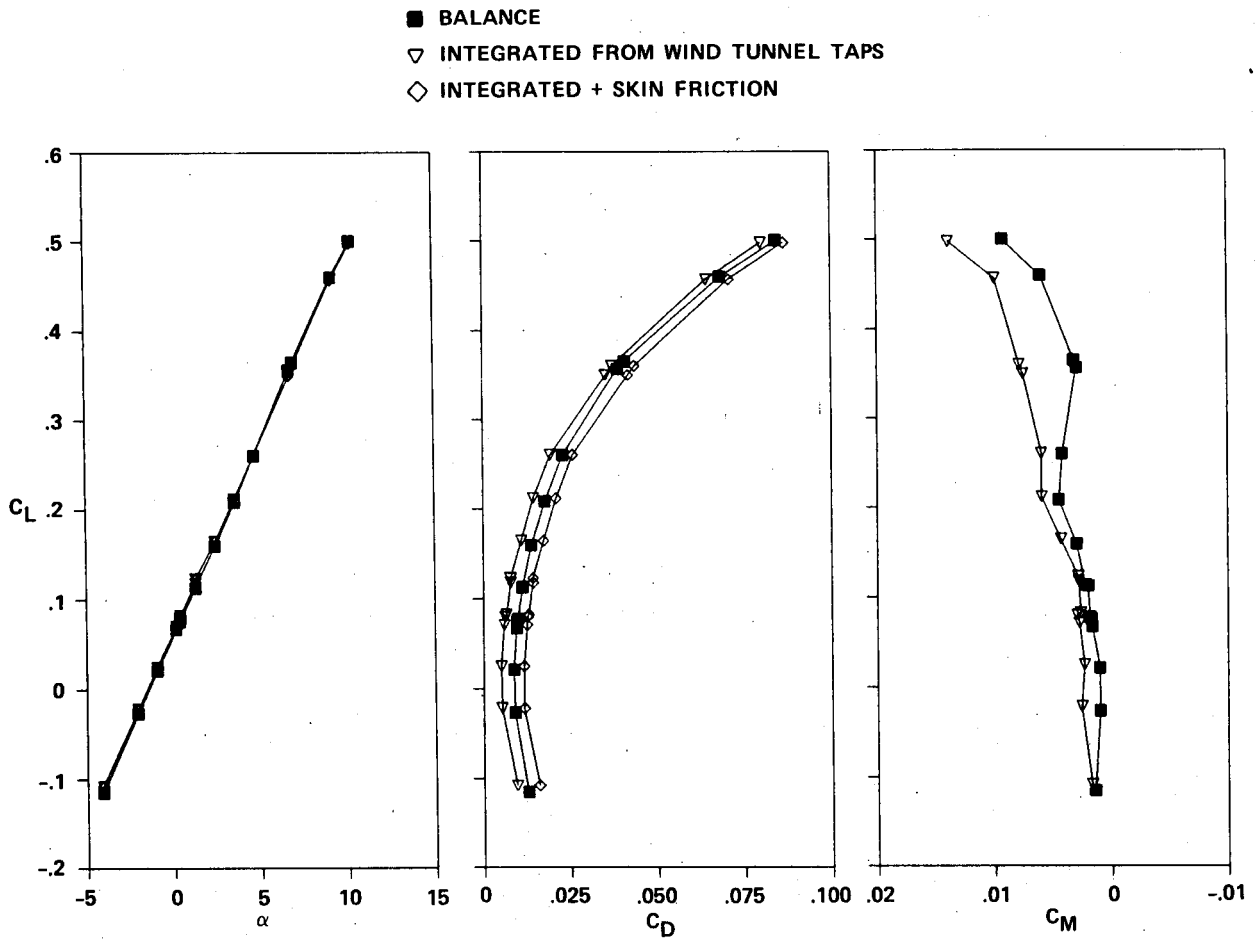


Figure 15.—Lift, drag, and moment data for  $M = 0.8$ .

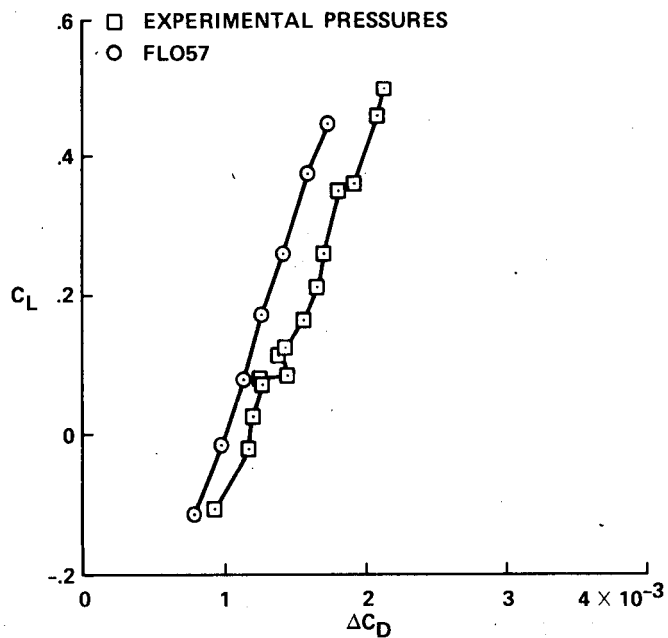


Figure 16.—Effect of removing the sting shroud on integrated drag,  $M = 0.80$ .

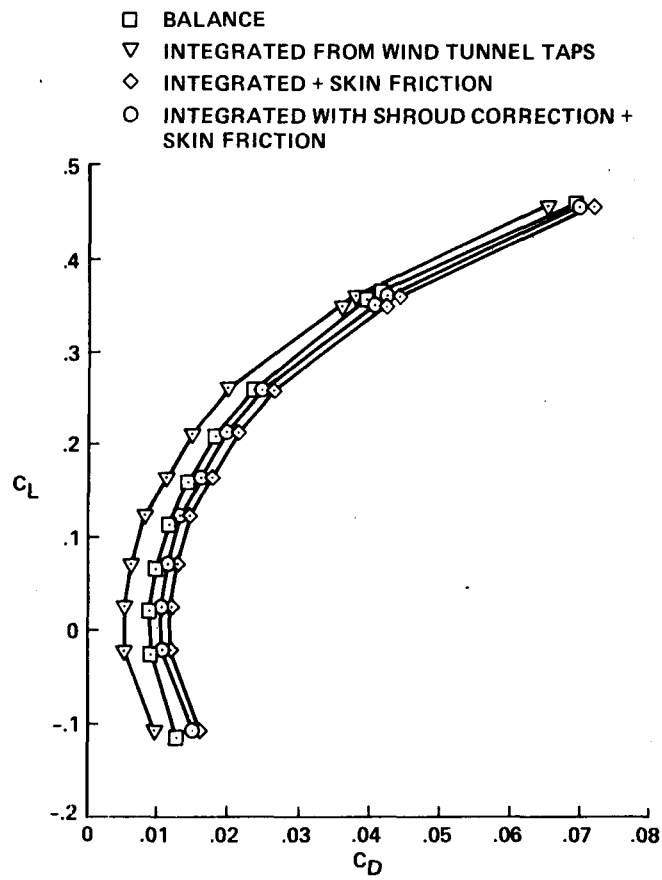


Figure 17.—Shroud increment removed from the  $M = 0.8$  drag polar.

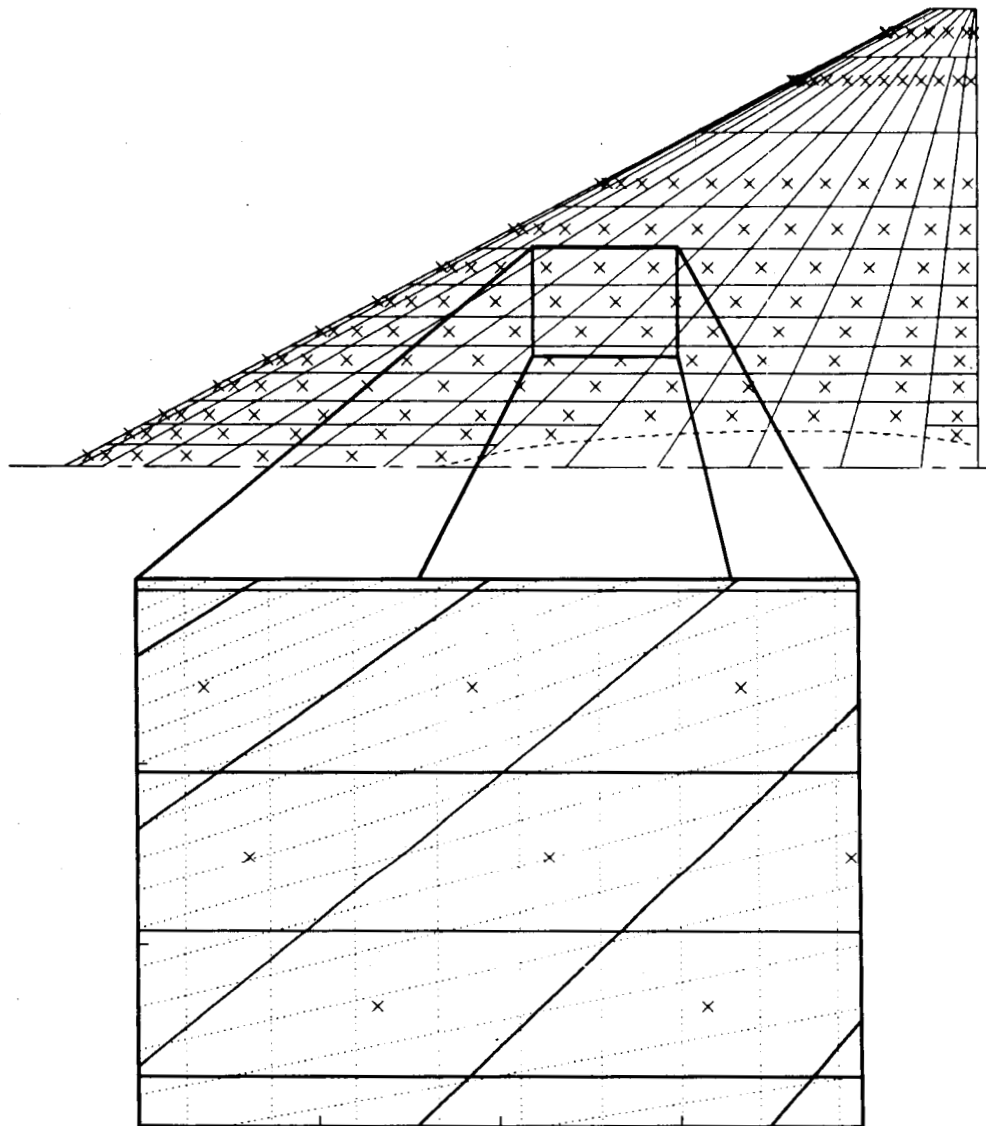


Figure 18.—Comparison between experimental and FLO57 grid.

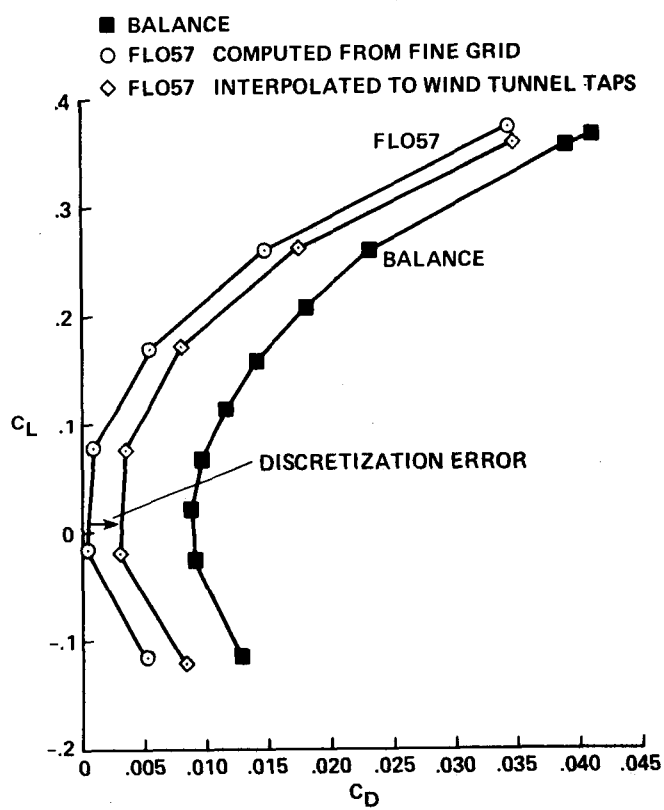


Figure 19.—Discretization effect on drag calculated from FLO57,  $M = 0.80$ .

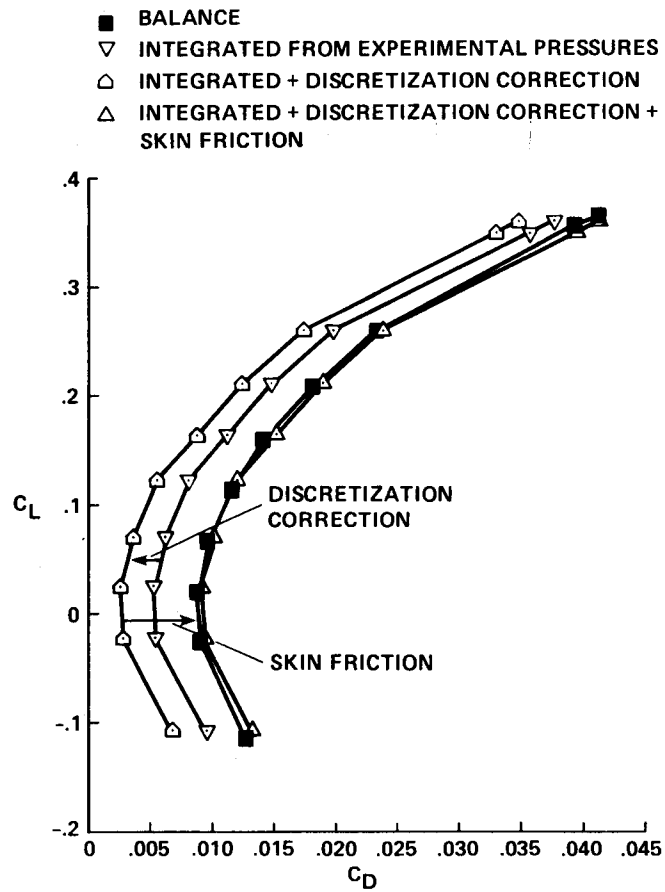


Figure 20.—Discretization correction determined from FLO57 applied to experimental data,  $M = 0.80$ .

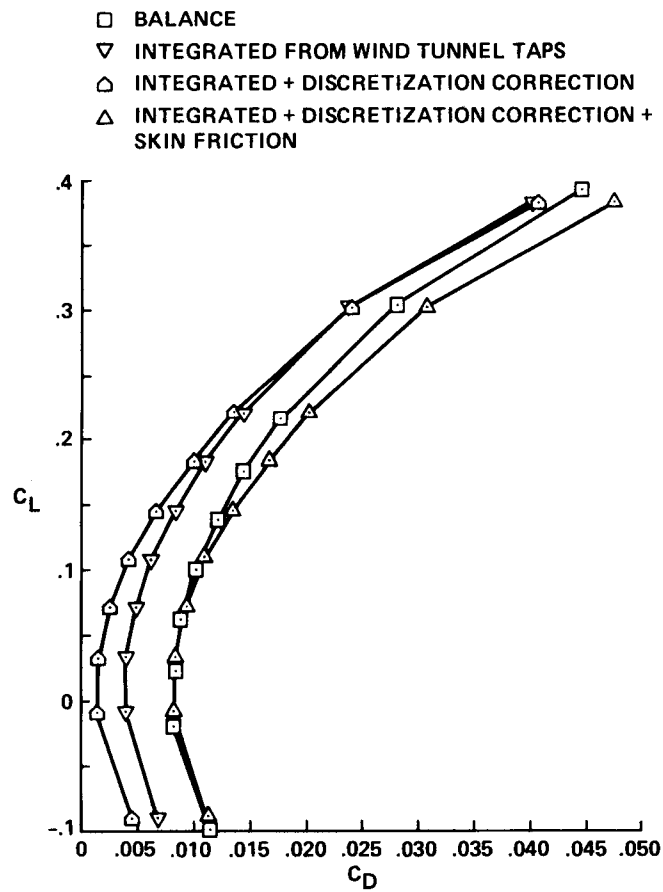


Figure 21.—Discretization correction determined from FLO57 applied to experimental data,  $M = 0.40$ .



# Report Documentation Page

1. Report No. NASA TM-102195		2. Government Accession No.		3. Recipient's Catalog No.	
4. Title and Subtitle An Integrated CFD/Experimental Analysis of Aerodynamic Forces and Moments			5. Report Date August 1989		
			6. Performing Organization Code		
7. Author(s) John E. Melton, David D. Robertson, and Seth A. Moyer			8. Performing Organization Report No. A-89145		
			10. Work Unit No. 505-61-91		
9. Performing Organization Name and Address Ames Research Center Moffett Field, CA 94035			11. Contract or Grant No.		
			13. Type of Report and Period Covered Technical Memorandum		
12. Sponsoring Agency Name and Address National Aeronautics and Space Administration Washington, DC 20546-0001			14. Sponsoring Agency Code		
			15. Supplementary Notes Point of Contact: John Melton, Ames Research Center, MS 227-6, Moffett Field, CA 94035 (415) 694-6208 or FTS 464-6208		
16. Abstract <p>Aerodynamic analysis using computational fluid dynamics (CFD) is most fruitful when it is combined with a thorough program of wind tunnel testing. The understanding of aerodynamic phenomena is enhanced by the synergistic use of both analysis methods. This report describes a technique for an integrated approach to determining the forces and moments acting on a wind tunnel model by using a combination of experimentally measured pressures and CFD predictions. The CFD code used was FLO57 (an Euler solver) and the wind tunnel model was a heavily instrumented delta wing with 62.5° of leading-edge sweep. A thorough comparison of the CFD results and the experimental data is presented for surface pressure distributions and longitudinal forces and moments. The experimental pressures were also integrated over the surface of the model and the resulting forces and moments are compared to the CFD and wind tunnel results. The accurate determination of various drag increments via the combined use of the CFD and experimental pressures is presented in detail.</p>					
17. Key Words (Suggested by Author(s)) Drag, CFD Delta wing, Wind tunnel experiments Euler equations			18. Distribution Statement Unclassified - Unlimited  Subject Category - 02		
19. Security Classif. (of this report) Unclassified		20. Security Classif. (of this page) Unclassified		21. No. of Pages 53	22. Price A04